




# The influence of laser power on the interfaces of functionally graded materials fabricated by powder-based directed energy deposition

Martina Koukolíková<sup>1,\*</sup> , Thomas Simson<sup>2</sup>, Sylwia Rzepa<sup>1</sup>, Michal Brázda<sup>1</sup>, and Jan Džugan<sup>1</sup>

<sup>1</sup>COMTES FHT a.s., Průmyslová 995, 334 41 Dobřany, Czech Republic

<sup>2</sup>Department of Mechanical Engineering and Environmental Technology, OTH Amberg – Weiden, Kaiser-Wilhelm-Ring 23, 92224 Amberg, Germany

Received: 13 April 2022

Accepted: 15 June 2022

Published online:  
18 July 2022

© The Author(s), under exclusive licence to Springer Science+Business Media, LLC, part of Springer Nature 2022

## ABSTRACT

Powder-based directed energy deposition (DED) technology with separate feeders for different individual materials enables the deposition of functionally graded materials (FGM) in combinations that would be very problematic using conventional technologies. These emerging innovative materials with the tailored properties of bimetallic material structures have potential applications in the energy, automotive and petrochemical industries. The combination of materials such as austenitic stainless steel 316L in combination with nickel superalloy Inconel 718 may satisfy requirements for corrosion and oxidation resistance, while maintaining suitable strength even at increased temperatures, at reasonable costs. However, the joining of dissimilar materials has certain limitations, and success depends on their mutual arrangement and the deposition parameters. The experimental program of the present study was aimed at optimizing the laser power of the powder-based DED process with respect to the quality of the interfaces of functionally graded materials in terms of microstructure evolution, interface quality and mechanical properties. One of the main objectives of the research was the analysis of two types of interfaces and the reduction in crack generation and propagation on the interface transition from Inconel 718 to 316L depending on the applied laser power, which ranged from 350 to 500 W. The presence of solidification cracks (SC) together with ductility dip cracking (DDC) played the most significant role in terms of the quality of this type of interface and significantly affected the values of the mechanical properties. Miniaturized tensile testing (MTT) in ZYX orientation at the individual interfaces' types throughout the deposit did not prove any dependence of the tensile characteristics on the sample position (bottom, middle

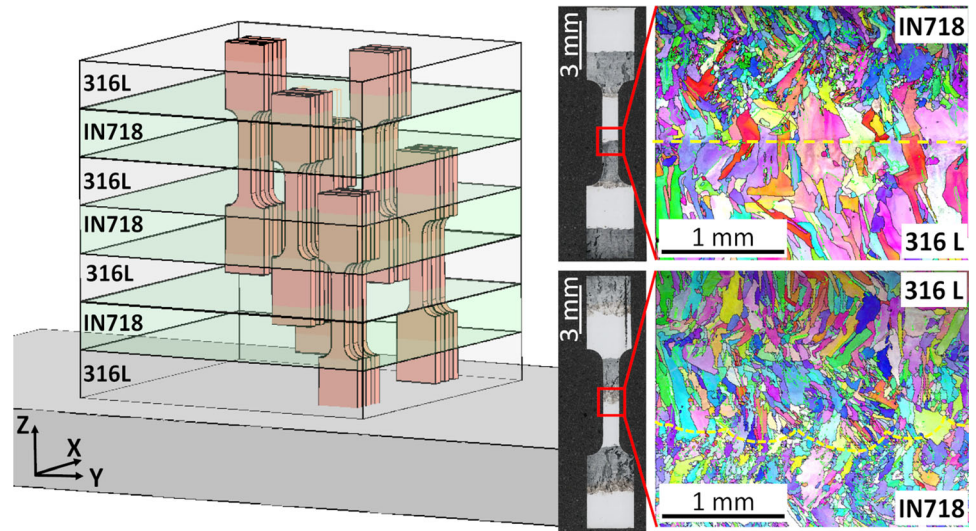
Handling Editor: Sophie Primig.

Address correspondence to E-mail: mkoukolikova@comtesfht.cz

<https://doi.org/10.1007/s10853-022-07453-9>

and upper part of the block), but were strongly associated with changes in the laser power. The results presented in this study prove that cracking at interfaces of functionally graded materials is minimized by optimizing the deposition process parameters, specifically the laser power. The research presents a promising application of nickel superalloy Inconel 718 on a 316L stainless steel substrate in a horizontal configuration.

## GRAPHICAL ABSTRACT



## Introduction

Additive manufacturing represents a collection of different technologies of component manufacturing methods for a wide range of industries with the greatest advantage of the possibility to produce

complex products with design and material freedom. The potentialities of additive manufacturing technologies such as directed energy deposition (powder- and wire-based) and laser powder bed fusion methods (L-PBF) to form metal components, and the interest in these advanced methods has grown enormously in recent years [1]. The principle of the powder-based

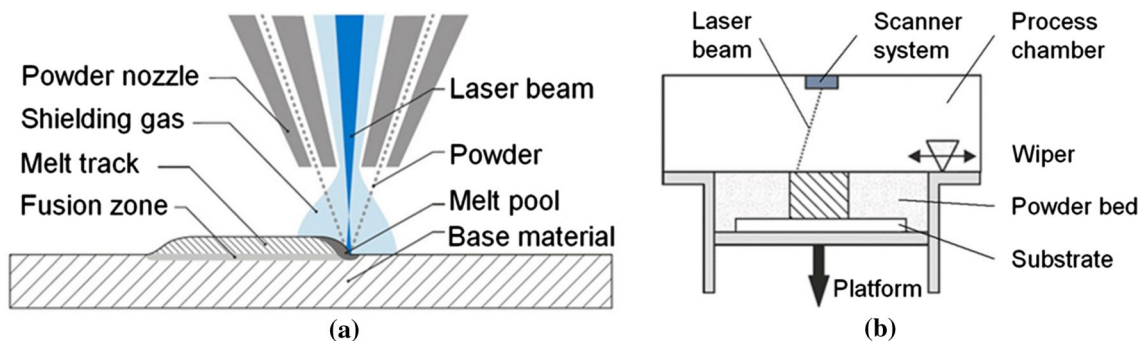


**Figure 1** Additive technologies: **a** powder-based DED; **b** laser powder bed fusion (L-PBF) [4].

DED technique (Fig. 1a) involves the laser beam to melt a material in form of powder, which is simultaneously deposited by a nozzle on the target surface. Layer thickness ranges from 250 to 900  $\mu\text{m}$  [2]. Whereas L-PBF methods (Fig. 1b) involve powder, which is placed on a platform in the form of a thin layer with a mechanical coating system, the top-most layer of the powder is selectively melted by a laser beam, and subsequently, the platform is lowered by the layer thickness, and the cycle is repeated. The typical layer thickness ranges from 30 to 50  $\mu\text{m}$  [3, 4].

Three main applications of powder-based DED have been identified: repairing, designing material and production in the energy, tooling, medical, automotive and aerospace sectors. DED can be used to repair damage to industrial equipment, which is usually characterized by complex shapes, such as turbo-engines, turbine blades, crankshafts, tools and moulds caused by component wear from exposure to operating environments with corrosion, thermal stress and variable thermal cycles and impact.

The great potential in the ability to repair using the DED technology compared to conventional methods such as tungsten inert gas welding (TIG) or arc welding lies in the lower heat input, residual stresses, warpage and distortions, and the higher precision in combination with significant cost and time saving could be achieved. Together with the individual deposition strategy, repairing of the above-mentioned components can lead to a significant increase in their lifetime. Another novelty of DED is a capability of deposition coatings on the surface of component, which are distinguished by specific properties like improved wear resistance or biocompatibility [1–8, 11].

The method enables relatively fast production of components, but it has poor surface quality and limited resolution in comparison with laser powder bed fused materials [9]. Unlike conventional laser powder bed fusion methods (L-PBF), powder-based DED can be used to repair damaged components of larger build volumes, and one of its advantages is that the surface of the base material does not need to be flat [5]. Using powder-based DED, additive manufacturing processes enable the production of larger components through the higher powder feed rate capability and build-up rates compared to the longer production times of powder bed layer deposition of L-PBF processes [1]. Both methods already allow the deposition of multiple materials in one work process [10].

The presence of functionally graded material interfaces is therefore a critical area that needs to be subjected to intensive research. The resulting microstructure plays an important role in terms of the final mechanical properties of the component and its possible industrial applications. One of the most challenging problems in repair is not only the different weldability of the functionally graded materials, but also the high content of basic and alloying elements, as there is a high tendency to form brittle phases [1, 11]. Cracks formed during solidification are often intergranular and have a dendritic structure due to the difference in solute concentration during solidification in the final stages of solidification [11, 12]. Precipitation and formation of carbides and Laves-phase occur at the end of solidification [13].

There is an enormous potential in the deposition of combinations of different materials. For example, the combination of 316L stainless steel and IN718 nickel superalloy materials offers a combination of materials with high oxidation and corrosion resistance with great potential for industrial applications [14]. Steel 316L is a chromium–nickel–molybdenum austenitic stainless steel, developed to provide good resistance to atmospheric corrosion and many organic and inorganic chemicals. The steel features high creep, stress-to-rupture and tensile strength at elevated temperatures. The low carbon content (max. 0.03%) ensures excellent resistance to intergranular corrosion in the as-welded condition, so no post-weld heat treatment is necessary [15]. The equilibrium microstructure at room temperature is austenitic, but rapid cooling during DED produces out-of-equilibrium structures. The complicated thermal history of additively manufactured components leads to various microstructures that can contain  $\gamma$ -austenite,  $\delta$ -ferrite and  $\sigma$ -phase [11, 16]. Stainless steel 316L is frequently used in the chemical and petrochemical industry, for food processing, power generation, construction, marine projects and also as a biomaterial for medical purposes. Inconel 718 is highly resistant to corrosion and is suitable for work in very hot and aggressive environments due to the high content of chromium and other alloying elements (such as aircraft components including combustion chambers and turbine parts) [17].

Due to the different temperature intervals of the solidus and liquidus of the steel and nickel alloys (316L: 1375–1440  $^{\circ}\text{C}$  and IN718: 1290–1350  $^{\circ}\text{C}$ , there is a relatively small difference between the thermal

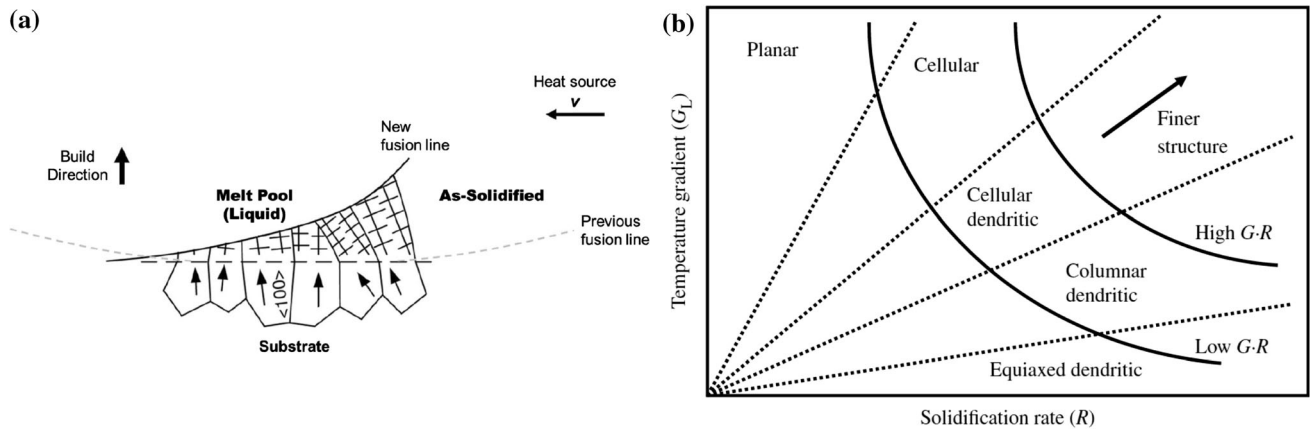


**Figure 2** a Epitaxial nucleation and competitive growth [24]; b effect of temperature gradient in the liquid  $G_L$  and solidification growth rate  $R$  on solidification mode [13].

expansion coefficient (CTE) value [14]. Despite this small difference, the crystallization of the individual alloys may be affected, as explored by Hinojos et al. in electron beam melting (EBM) and Mohd Yusuf with L-PBF additive manufacturing [18, 19]. The austenitic matrices crystallize in a cubic face centred lattice (FCC) and the lattice parameters of the main elements, i.e. Fe for 316L stainless steel and Ni for IN718 nickel superalloy do not differ much (Fe:  $a = b = c = 3.65$  [Å]; Ni:  $a = b = c = 3.56$  [Å]).

Austenitic stainless steels and nickel-based superalloys are generally susceptible to three crack mechanisms during welding, i.e. solidification cracking, ductility dip cracking and liquation cracking [13, 20]. The metallographic identification of SC-type cracks is relatively straightforward because crack propagation occurs along solidification grain boundaries (SGB) with high angular misorientation. These are often called “high-angle” grain boundaries (HAGBs) with misorientation angles  $> 15^\circ$ . Crystallographic misorientation across subgrain boundaries, attributed to the dense cellular (columnar or equiaxed) substructures, represent low-angle boundaries (LAGBs) having misorientation angles from  $2^\circ$  to  $15^\circ$  [13, 19]. DDC is always intergranular, usually associated with large grain and generally refers to the sharp reduction in ductility that susceptible materials exhibit in a temperature range between the alloy solidus and approximately half the solidus temperature. (For stainless steels and Ni-base alloys, the range is between 800 and 1150 °C.) Deformation concentration occurs at the grain boundaries as the strain localization in materials with FCC lattice gives rise to grain boundary sliding and preferential void formation and cracking at the grain boundaries [13].

The incidence of this type of cracks in conventionally welded IN718 and 316L multimaterials was eliminated by the use of filler materials [21]. Additive manufacturing can avoid the use of filler materials and can ensure a high-quality metallurgical joint while minimizing thermal damage to the surrounding material [18].

The additive manufacturing of FGM materials results in a different solidification behaviour compared to the deposition of individual materials, which is due to the complex physics of mass and heat transfer in a melt pool, caused by convection of the liquid at the bimaterial interface [22]. Grain formation during powder-based DED is initiated by the epitaxial nucleation of grains and proceeds by the mechanism of competitive growth [23, 24], (Fig. 2a). The newly formed grains retain the same crystallographic orientation as the grains of the base metal from which they were formed. As a result, the grain boundaries are continuous across the melting boundary [13]. Depending on the temperature gradient in the melt, the solidification growth rate and the solidification mode, planar, cellular and dendritic growth modes are observed in the stainless steel and nickel superalloy functionally graded materials fabricated by conventional welding and also AM technologies (Fig. 2b) [13, 16, 20].

Hallberg et al. [12] studied the effect of the depth-to-width ratio of the melt pool with an interesting approach to reducing the formation of solidification cracks in nickel-based superalloys processed by laser powder bed fusion. Their research work claims that as the melt pool solidifies, residual stresses may form at the melt pool boundaries due to shrinkage. In

deeper and narrower meltpools, higher residual stresses are generated. Typical solidification cracks at the solidification front in the meltpools are located at the point where the last liquid in the meltpool solidified. This localization of deformation is the cause of the shift at the grain boundaries and the preferential formation of void formation and cracks at the grain boundaries.

The work of Zietall and Feenstra confirmed that in materials with an FCC lattice, precipitation occurs at the end of solidification, which results in embrittlement in the additive production of stainless steel and Inconel alloys during welding. As the Fe content in the interface layers increases, the solubility of Mo and Nb in the austenitic matrix decreases, thus increasing the susceptibility to the formation of detrimental phases such as Laves phase (Ni, Fe, Cr)<sub>2</sub> (Nb, Mo, Ti) and NbC carbides [25]. Works focused on the combination of stainless steel (316L) with nickel alloys (Inconel 617/Inconel 625/Inconel 718 (IN718)) fabricated by powder-based directed energy deposition system, concentrated mainly on structural integrity, mechanical properties, microstructural characteristics, crack formation and thermodynamic modelling [14, 16, 25–28].

The authors Meng, Li, Han, and Zhang [27–31] mainly deal with additive manufacturing of functionally graded materials fabricated by powder-based directed energy deposition and laser powder bed fusion, focusing on cracking behaviour, mechanical properties and microstructural characterization. In Meng et al. [29], their work focuses on fabricating 316L/Inconel625/Ti6Al4V gradient material with synchronous preheating, finding that a key indicator of gradient materials is the reduction of Nb-, Mo-, Cr-enriched eutectic phase formation, and uneven temperature field distribution. The main achievements in the powder-based DED production of FGMs using steel and Inconel were successfully used in order to improve the wear and corrosion resistance in the automotive sector [1].

According to the literature data devoted to FGM, researchers studied the influence of different material composition [32, 33], effect of synchronous preheating [28] and various laser power (in range 450–750 W with 100 W step) on the microstructure and mechanical properties of additively manufactured components. The current study is the first investigation, where FGM (316L–IN718) is deposited with different laser power values ranging from 350 to

500 W with step of 50 W including innovative DMT mode and subjected to detailed microstructural analysis. The novelty aspect of this investigation is an application of DMT mode and comparison of the properties with the builds deposited with constant laser parameters. Many powder-based DED systems are produced without this feature, which means that components can be deposited only with constant laser power. In the case of the machine employed in current study, the value of laser power is adjusted with high frequency according to the layer height monitored by two vision cameras.

The research presented in this manuscript explores the effects of changes to the applied laser power on the quality of individual interfaces, mechanical properties and the microstructure of functionally graded material blocks of 316L/IN718. Light microscopy (LM), scanning electron microscopy (SEM), grain and texture characterization (via electron backscatter diffraction) provided deep insight into the microstructure of the FGM materials. The metallographic analysis was supported by the results of miniaturized tensile test. The miniaturized specimen testing can be successfully applied in order to characterize local properties of the component or when little amount of material is available for testing [34–36]. The reliability of this methodology was investigated by many researchers [34–43]. They concluded that testing results can be affected by too low number of grains along the specimen's thickness and specimen geometry including its proportionality according to standards. If these requirements are satisfied, the values of obtained tensile characteristics can be directly compared with the results of standard testing. The aim of this study was to reduce the amount of defects, primarily micro-cracks, in a powder-based DED processed FGM materials. In order to select the deposition parameters, namely the laser power that ensure minimal number of defects and enhancement of mechanical performance, the detailed analysis of microstructure and mechanical behaviour is crucial. The enormous amount of testing provided insight into the properties of the functionally graded materials.

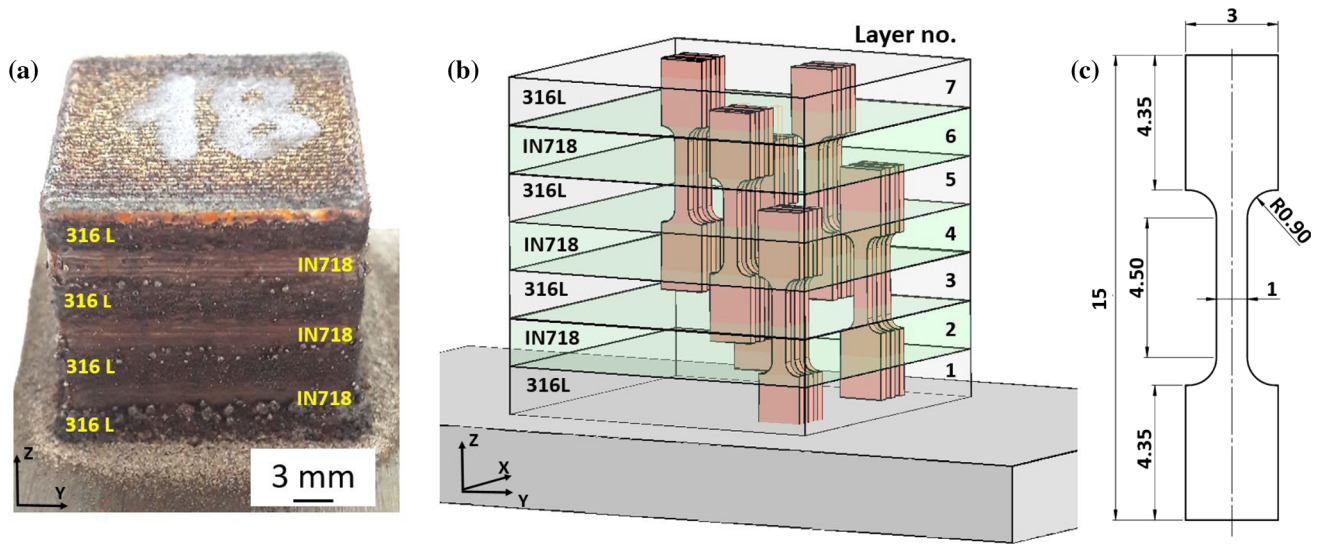


**Figure 3** MTT samples: **a** Block deposited using DMT mode with marked layers; **b** cutting scheme; **c** geometry of miniaturized tensile test specimen.

**Table 1** Process parameters for powder-based DED

Material	Process parameters				
	Laser power (W)	Powder feed rate (g/min)	Module	Beam diameter ( $\mu\text{m}$ )	Feed rate (mm/min)
316L	350, 400, 450, 500, DMT	3.0	SDM 800	800	849
IN718	350, 400, 450, 500, DMT	2.3			

## Materials and methods

The functionally graded material blocks (Fig. 3a) were fabricated by powder-based DED using the INSTEK MX-600 system (InssTek, Daejeon, Korea), which is equipped with a 2 kW Yttrium fibre laser. The layers of 316L stainless steel (Sandvik Osprey Ltd., Sandviken, Sweden, Batch: 20D0325) and nickel superalloy Inconel 718 (AP&C, Quebec, Canada, Batch: 191-A0379) were deposited in the horizontal orientation in 3-mm alternating layers. The average particle size of the powders of 316L was 53–150  $\mu\text{m}$ , and of IN718 was 45–150  $\mu\text{m}$ . The dimensions of the blocks were 21  $\times$  21  $\times$  21 mm. The powders were fed from separate feeders to the nozzle. The first layer of 316L was created on a heat-treated platform made of 316L. To allow comparison of the mechanical properties and the microstructure, two blocks were deposited from individual materials, i.e. from 316L steel (designated as 316L) and Inconel 718 (designated as IN718) in the direct metal tooling (DMT)

mode. The DMT mode was used in the present study to gain an initial understanding of the behaviour of individual materials and to determine the range of laser power for the production of gradient materials. DMT technology analyses and controls the height of the melt pool in real-time using two vision cameras, which are used to monitor the distance of the melt pool from the laser nozzle at ideal distance of 9 mm. The laser power is adjusted several times per second to maintain a continuous layer, and if the distance is less than 9 mm, the power is automatically reduced and vice versa. Subsequent application of fixed powers for both materials ensured the same thermal input conditions.

The aim of this study is to investigate the effect of the applied laser power on the quality of individual interfaces of FGM materials from the perspective of the application of 316L stainless steel to IN718 and vice versa.

The process parameters are summarized in Table 1. The scanning strategy was the zig-zag (ZZ) method

with 90° rotation of individual layers. The height of the deposited layers was 0.25 mm with a width of 0.8 mm and a hatch distance of 0.5 mm. Applied laser power ranged from 350 to 500 W in 50 W steps and in automatic DMT mode (range from 375 to 450 W). The lower power limit (350 W) was chosen to guarantee the powder melting of the individual materials, and the upper limit of 500 W was chosen to increase the power above the upper limit of the DMT mode, which is 450 W. Shielding argon gas at a rate of 5 L/min was fed around the laser and powder path to avoid oxidation.

Samples were cut in the YZ plane, i.e. the plane parallel to the Z printing (building) direction. Conventional metallographic preparation involved grinding and subsequent polishing using a standard metallographic procedure (final steps—Nap 1  $\mu\text{m}$  + OP-S Non-Dry colloidal silica suspension 0.25  $\mu\text{m}$ ) performed on an automatic, microprocessor-controlled machine for grinding and polishing specimens Tegramin 30 (Struers GmbH, Ballerup, Denmark). The microstructures were revealed by etching at elevated temperatures in V2A solution and photographed using a Nikon Eclipse MA200 (Nikon, Tokyo, Japan) light microscope (LM) equipped with NIS Elements 5.2 digital image processing and analysis software (Nikon, Tokyo, Japan). Detailed microstructural observation and electron backscatter diffraction (EBSD) were performed on a JEOL IT 500 HR (JEOL Ltd., Tokyo, Japan) scanning electron microscope with an EDAX Hikari Super camera (EDAX LLC, Mahwah, NJ, USA). EBSD maps were processed in 50  $\times$  magnification with a step size of 5  $\mu\text{m}$ , analysed area 2560  $\times$  2000  $\mu\text{m}$ , acceleration voltage 30 kV, scanning speed 100 points per second and 5  $\times$  5 binning. The data acquisition, analyses and post-processing were performed using the software TEAM 4.5 (EDAX LLC, Mahwah, NJ, USA) and EDAX OIM Analysis<sup>TM</sup> Version 8.0 (EDAX LLC, Mahwah, NJ, USA).

Hardness profiles HV1 were measured using a Struers DuraScan 50 (EMCO-TEST Prüfmaschinen GmbH, Kuchl, Austria) laboratory hardness tester equipped with ecos Workflow<sup>TM</sup> software (EMCO-TEST Prüfmaschinen GmbH, Kuchl, Austria). Hardness profiles were measured according to ISO 6507-1 over the whole block from the top towards the platform across the individual interfaces with a step of 1 mm.

The tensile properties were investigated using a miniaturized tensile test (MTT). This type of testing is now common practice, and the applicability of MTT has been reported in many studies [34–43]. MTT specimens were tested in ZYX orientation (marked according to ASTM WK49229—Standard guide for Orientation and Location Dependence Mechanical Properties for Metal Additive Manufacturing) and marked with the number of the layer from where they were extracted. The interface was always placed in the centre of the test body, i.e. the samples were taken from the interfaces between the layers 2–3, 3–4, 4–5, 5–6. The cutting scheme of MTT samples is shown in Fig. 3b. Interfaces 2–3 and 4–5 are interfaces from IN718 to 316L stainless steel (marked interface II) and interfaces 3–4 and 5–6 from 316L stainless steel to IN718 (marked interface I). Six specimens were cut from each block according to the scheme shown in Fig. 3c using a wire electrical discharge machine (WEDM). Prior to testing, each specimen was polished to the required roughness. At least three specimens were tested in specific, predefined conditions. The testing procedure followed the ISO 6892-1 standard. All specimens were tested under quasi-static conditions (a strain rate of 0.00025  $\text{s}^{-1}$ ) at room temperature. The experiment was conducted using a TiraTest universal testing machine with a linear drive and a load capacity of 10 kN. The device was equipped with grips designed for sub-sized specimen testing. The specimen deformation was tracked by contactless system Mercury RT based on Digital Image Correlation calibrated in 2D mode with one camera. The measurement method is characterized by high accuracy of  $> 0.01\%$ . The specimens were cleaned with an agent based on alcohol, and a stochastic black-white pattern was prepared on the surface for contactless deformation tracking. In order to ensure the proportions of the samples, the initial gauge length of the virtual extensometer was chosen as  $L_0 = 4$  mm. After the testing, the specific specimen dimensions were measured again using a stereomicroscope. Based on the results, the tensile characteristics of the experimental material were calculated as YS (0.2% offset yield strength), UTS (ultimate tensile strength), UE (uniform elongation), El (total specimen elongation) and RA (reduction of the cross-sectional area) of the experimental material.

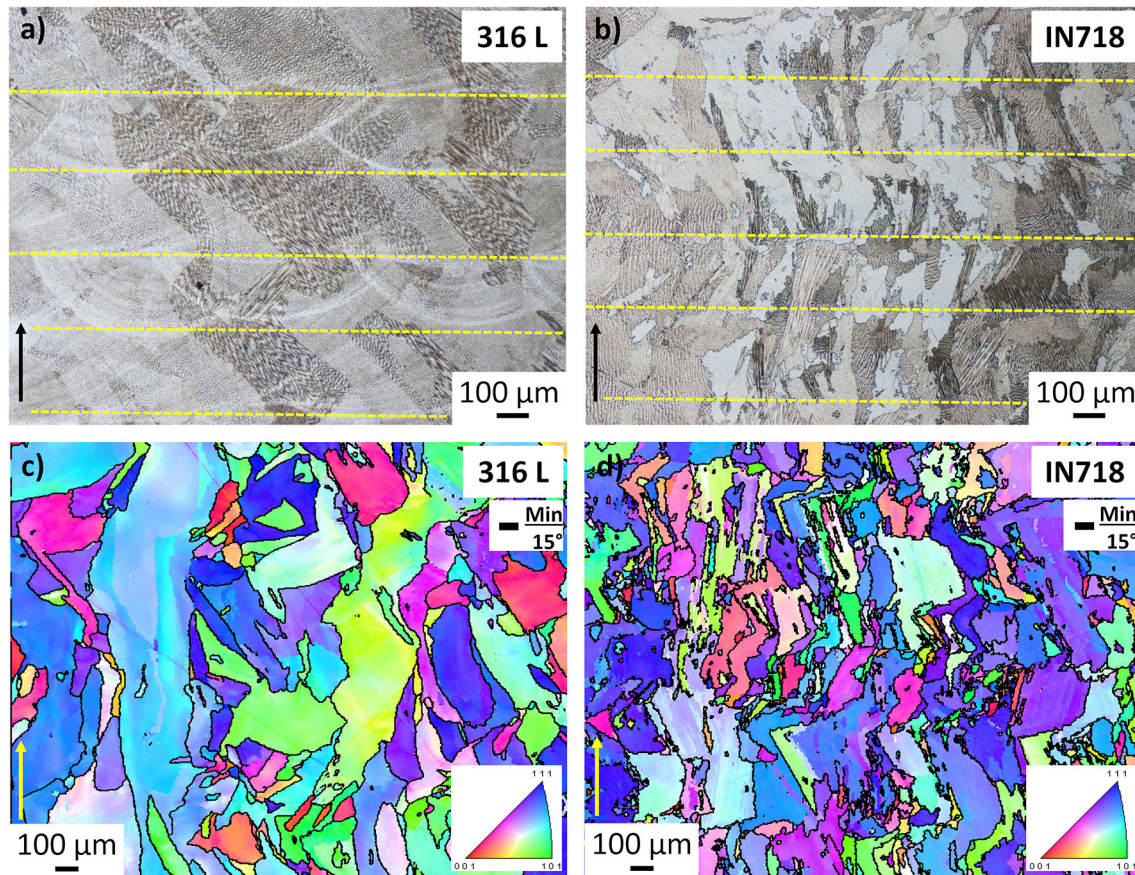


**Figure 4** Microstructures of individual materials: **a** LM—316L; **b** LM—IN718; **c** EBSD—316L IPF map; **d** EBSD—IN718 IPF map. Arrow indicates the building direction (Z).

## Results

### Microstructural features

In the microstructure of 316L steel, the presence of either pure austenite or a two-phase microstructure of austenite with delta-ferrite can be expected. In order to predict the delta-ferrite presence in the austenitic stainless steel, Schaeffler and De Long structural diagrams may provide an information on the structural composition; however, the occurrence of the different phases and the proportion in which they are represented in the steel structure depends in addition on the chemical composition, process conditions and the method of metal deposition [44]. Recent investigations [45–49] into the development of the microstructure in AM 316L observed a fine subgrain structure forming inside columnar austenite grains. The microstructure in these studies consists of FCC austenite phase and BCC delta-ferrite phase on the subgrain and grain boundaries.

The austenitic matrices crystallize in a face-centred cubic (FCC) lattice and the lattice parameters of the base elements, i.e. Fe and Ni, do not differ significantly. The base materials printed in DMT mode exhibited different grain sizes. Metallographic analysis proved the microstructures of additively manufactured stainless steel and nickel superalloy exhibited different trends in grain size and orientation with respect to the printing direction. The microstructures of the 316L stainless steel and IN718 nickel superalloy base materials observed by light microscopy are shown in Fig. 4a,b. The samples were cut and analysed in the YZ plane, the arrow indicates the building direction (Z), and individual printing layers are highlighted with yellow dashed lines. The microstructure of both materials exhibited the presence of columnar grains, which are the result of partial remelting of the previously applied layer enabling the previous grains to serve as nucleation sites for solidification of the following layer [50].



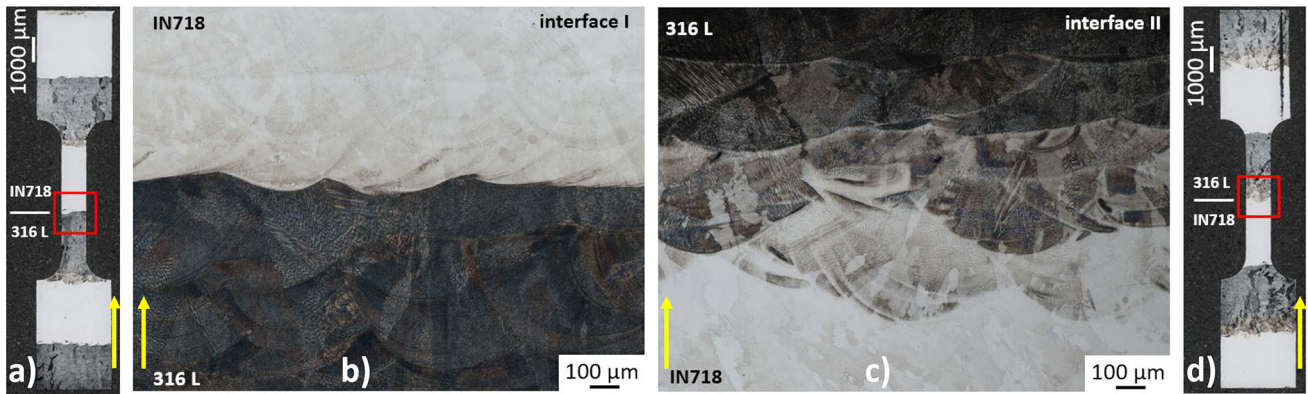


**Figure 5** Types of interfaces: **a** MTT specimen at interface I; **b** interface I microstructure; **c** interface II microstructure; **d** MTT specimen at interface II. Arrow indicates the building direction (Z).

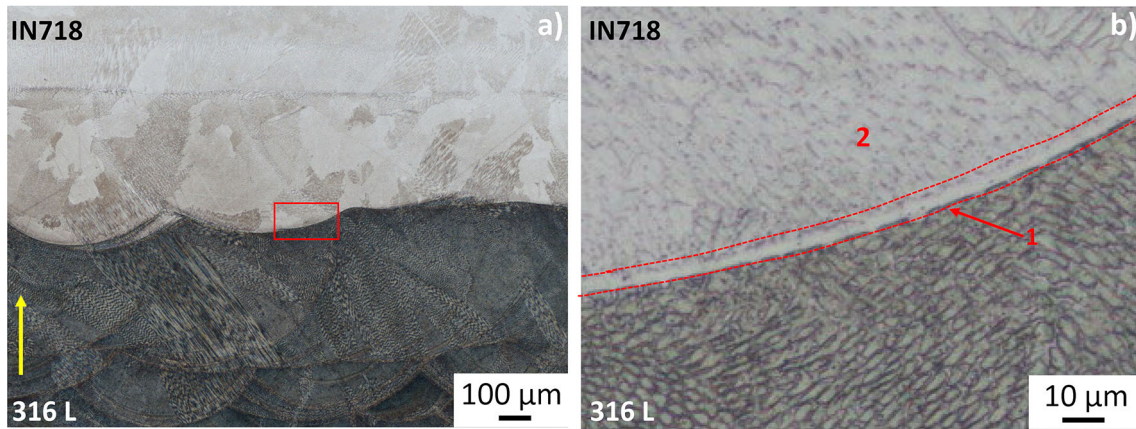


**Figure 6** Interface I microstructure: **a** applied laser power 450 W; **b** detail of the planar growth region. Yellow arrow indicates the building direction (Z).

As Mohd Yusuf referred in study [19], differences in CTE of IN718 and 316L influence the crystallization of individual alloys. The lower CTE coefficient of the nickel alloy limits the expansion area and volume of solidified grains within a given temperature gradient. The EBSD inverse pole figure (IPF) maps shown in (Fig. 4c, d) captures the differences in the grain morphology. The columnar grains of 316L reached a coarse-grained character, reaching up to several subsequent layers height. The grains of IN718 have a finer character, and the count of smaller grains is higher. The crystallization of grains in both materials has a distinct tendency to follow the direction of heat flow using the zig-zag DMT mode strategy.

Two types of interfaces were detected in the functionally graded material samples produced by powder-based DED. These interfaces have been already investigated in previous works by Melzer, Dzugan and Li et al. [14, 23, 27, 51]. These interfaces are

**Table 2** Effect of applied power on meltpool depth

Power	Meltpool depth (μm)			
	Interface I	Interface II	316L	IN718
350	240.7	292.3	292.2	276.1
500	337.1	435.6	354.1	335.4
DMT	306.0	487.8	326.8	288.6

referred to as interface I and interface II. Interface type I was detected at the 316L stainless steel to IN718 interface, and interface type II at the IN718 to 316L stainless steel interface. When austenitic stainless steel transitions to nickel superalloy (Fig. 5b), interface I is characterized by a sharp interface. In interface II, there is a gradual change of the individual materials with a gradient change in chemical composition (Fig. 5c). Figure 5a and d shows the

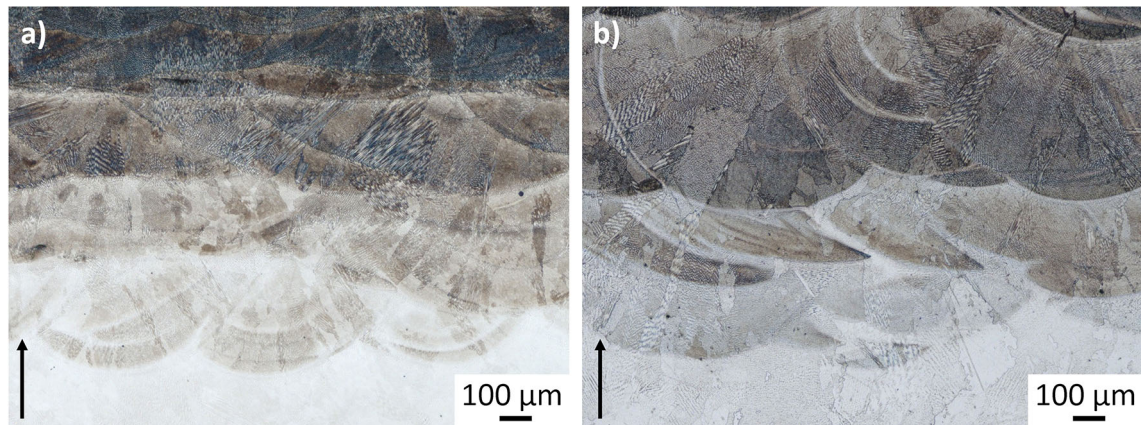


**Figure 7** Shape and size of melt pools at the interface II: **a** 350 W; **b** DMT. Arrow indicates the building direction (Z).

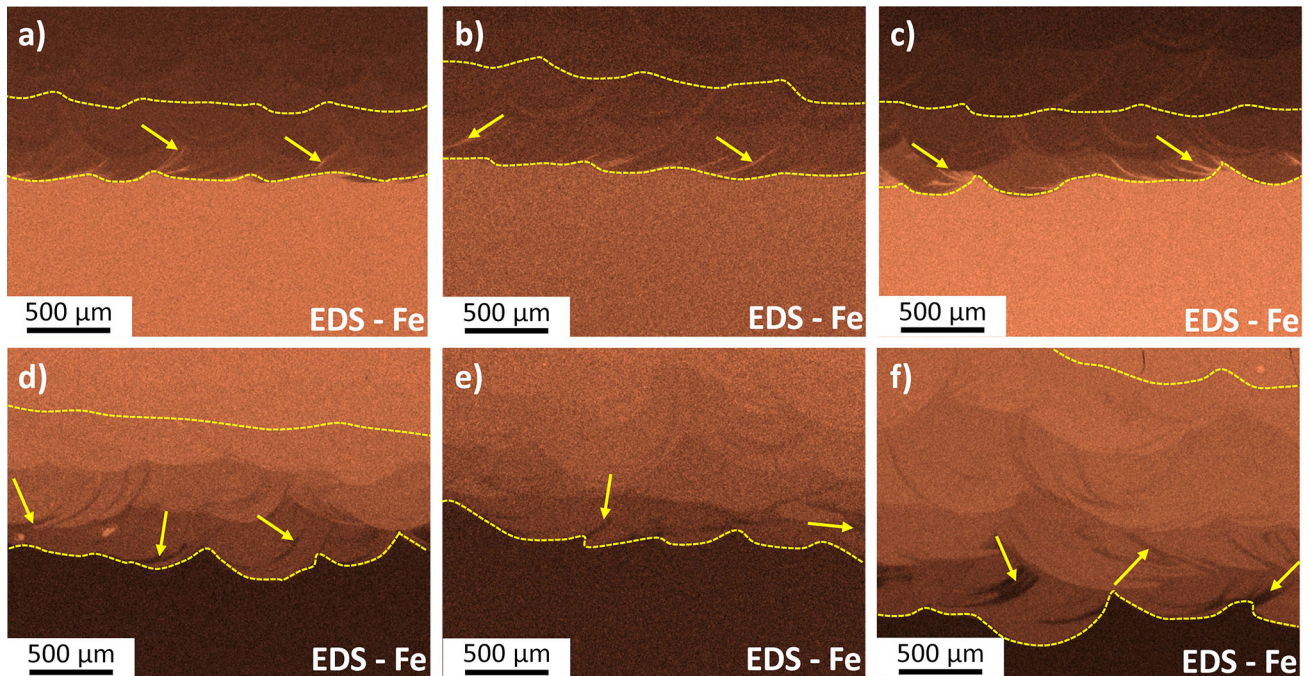


**Figure 8** EDS analysis of the Fe mapping at the interface: **a** 350 W-I; **b** 500 W-I; **c** DMT-I; **d** 350 W-II; **e** 500 W-II; **f** DMT-II.

metallographic samples of miniature specimens for microtensile testing. In the tested region, the interface was always placed in the centre of the test body (highlighted by the red square).

Type-I interface depicts a shallower penetration than the type-II interface. The presented observation indicates that 316L undergoes more remelting than nickel-based alloy at the interface II, and this difference can be explained by the lower energy absorption rate and lower thermal conductivity of IN718 relative to 316L. This is in agreement with the observations in Fig. 5 and previous studies of Chen and Xiao [16, 22],

which demonstrated the powder-based DED deposition of bimetal material IN625/SS316L enhanced with numerical simulations of flow fields within the melt pool of individual interfaces.

The detailed metallographic analysis (Fig. 6a) of the type I interface (referred to as the transition zone (TZ) by Lippold [13] was characterized by a planar growth region (Fig. 6b—locality 1). The planar growth region evolved as a function of the ratio of the temperature gradient  $G$  to the growth rate  $R$  (Fig. 2b), leading to a relatively large  $G/R$  value which facilitated the planar growth at the onset of solidification

[52]. This type of transition at the fusion boundary rapidly breaks down into a cellular and dendritic solidification growth region (Fig. 6b—locality 2) as a result of gradually decreased  $G$  and increased  $R$ , which was observed in all samples regardless of applied laser power.

Using the DMT deposition mode, due to the unstable process and laser power and the effort to keep the nozzle ideally at a distance of 9 mm from the surface of the deposited material, irregular melting of individual layers and irregular shapes of individual meltpools occurred. This effect was most apparent at interface II, while at interface I, this phenomenon did not manifest itself significantly. In the area of the material itself, the dimensions of the meltpools stabilized as summarized in Table 2 for 350 W, 500 W and DMT mode. The constant power of 350 and 500 W in the analysed materials enabled the creation of meltpools with a more regular shape and a more stable height than in the case of the DMT mode (Fig. 7). The higher power, i.e. 500 W, caused a greater melt depth due to the higher energy input and the associated larger size of the meltpools.

Since iron is one of the main elements of the steel and its content is diametrically different in these two alloys, the Fe content at each interface was also monitored by EDS analysis (Fig. 8). Unmixed zones (UMZ) were observed at both interfaces. These are areas of the fusion zone (FZ—highlighted by yellow dashed lines) immediately adjacent to the fusion boundary which have a slightly different composition from the adjacent weld metal due to evaporation or contamination [13] as the solute mixing in this transition zone is insufficient, and the inhomogeneity of the local composition is still preserved. Complex convection flow inside the meltpool, observed by Dang et al. [52], is driven by different forces including surface tension gradients, recoil pressure and

buoyancy. The fluid flow in the meltpool and the temperature gradient along the fusion boundary both have a significant effect on the creation of UMZ. If the fluid flow is intense, UMZ “mixes” into the weld metal. The temperature gradient at the fusion boundary can affect the UMZ width [12, 13]. The UMZ areas highlighted by arrows are characterized by lighter sites in the first layer application area at interface I (Fig. 8a–c) and darker sites in the first layer application area at interface II (Fig. 8d–f). In particular at interface II, the observed UMZ interfered not only in the first layer, as was the case at interface I.

The average widths of the FZ and UMZ were measured for selected laser powers 350 W, 500 W and DMT mode. The results are summarized in Table 3. The width of the UMZ was measured in two examples. The measurements proved that there is an increase in FZ width with the application of higher power. This is most noticeable at interface II. Using DMT and the associated unstable process and irregular melting of individual layers, the width of FZ was most noticeable.

### Cracking behaviour at interface II

A detailed metallographic analyses detected the presence of defects originating from the solidification cracking (SC) and ductility dip cracking (DDC) in the fusion zone at the interface II. The defects were already present during the application of the second to the third layers of the material. The mechanism of crack formation in the present study can be attributed to several factors. These are a natural shrinkage during solidification which contributes to residual stresses; thermal stresses induced via different CTE between the alloys; the incidence of liquid films which are present along the grain boundaries during solidification in the fusion zone and which can persist up to temperatures significantly lower than the equilibrium temperature of the alloy solidus; changes in chemical composition [13, 18, 22]. The metallographic identification of SC was relatively straightforward as cracks followed the solidification grain boundaries (SGB) and tend to have a wavier appearance (Fig. 9). Also, there is considerable liquid film evident along the solidification crack path at the end of solidification [13]. Fractographic features of the cracks were observed in chapter 3.5 Fractographic analysis.

**Table 3** Measured width of FZ and UMZ

Interface	Width ( $\mu\text{m}$ )		Interface	Width ( $\mu\text{m}$ )	
	FZ	UMZ		FZ	UMZ
350W_I	446	13	350W_II	929	34
		28			27
500W_I	523	21	500W_II	1300	50
		32			37
DMT_I	499	19	DMT_II	1448	132
		14			57

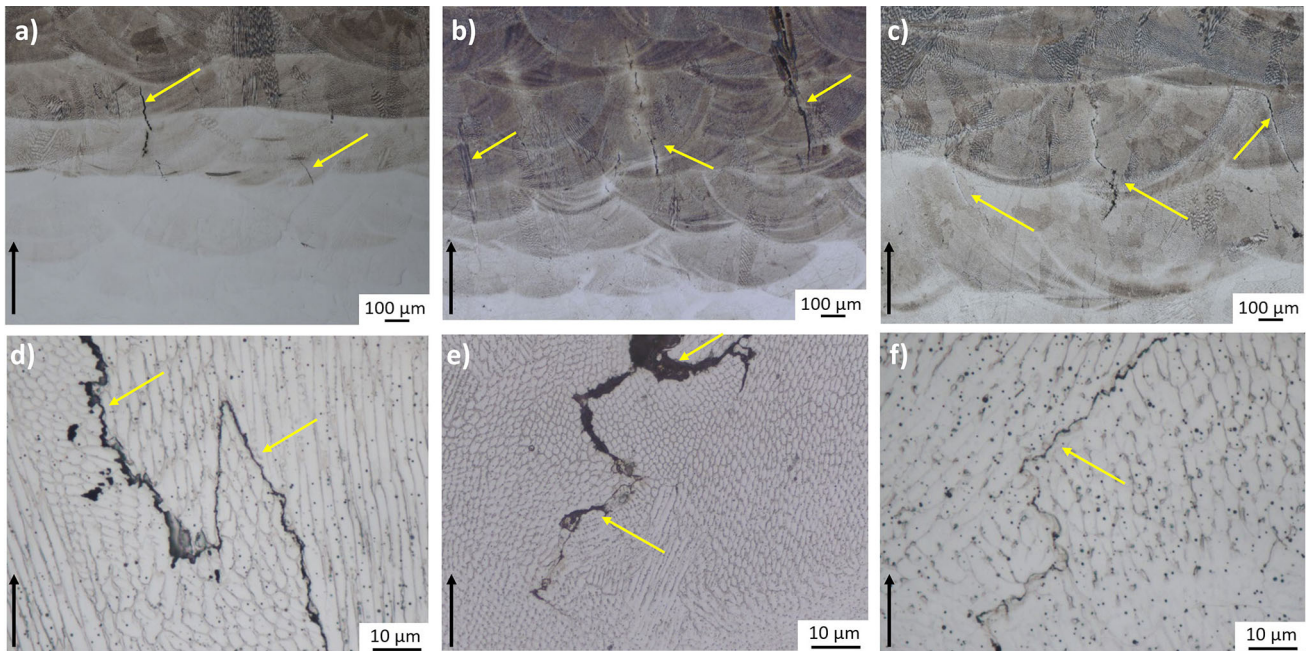


**Figure 9** Solidification cracking at interface II: **a** 350 W; **b** 500 W, **c** DMT; **d** 350 W crack detail **e** 500 W crack detail; **f** DMT crack detail. Cracks are highlighted with yellow arrows.

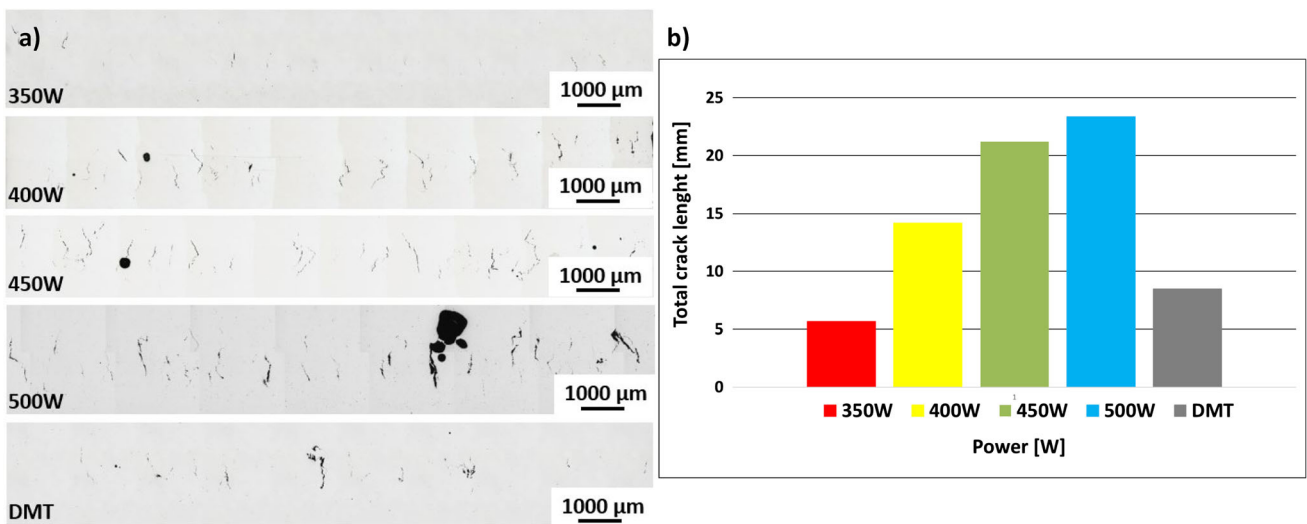


**Figure 10** **a** Presence of cracks detected in the material with different laser powers; **b** Dependence of total crack length on the laser power.

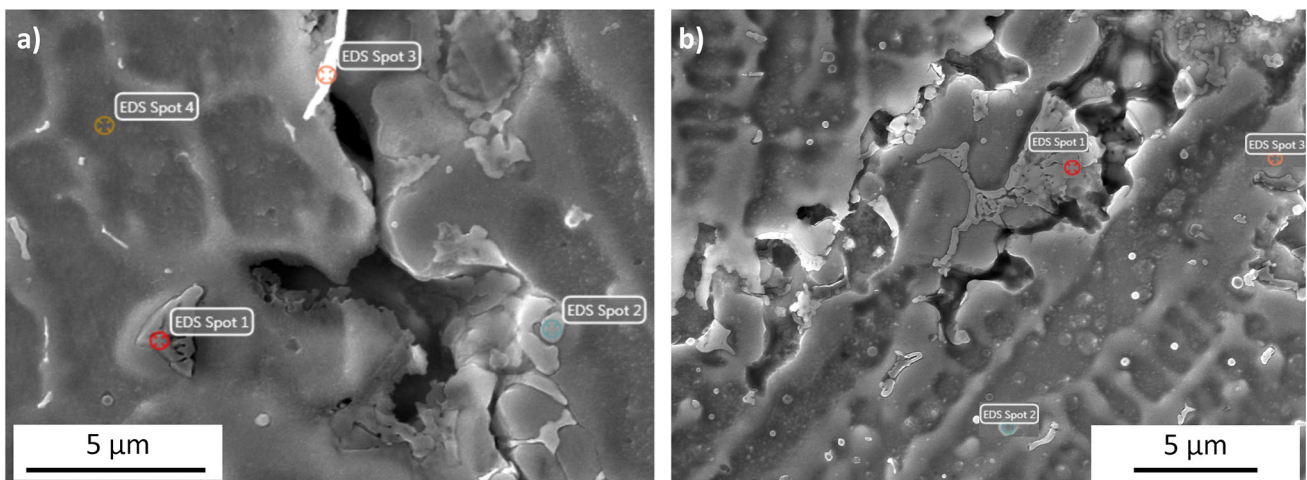
Crack propagation occurred along the grain boundaries with their lengths exceeding the height of several layers. At 350 W, small cracks at interface II were detected from layer 2 onwards (Fig. 9a). These are really fine cracks without massive propagation, extending over a maximum of two layers, directed to the centre of the shallow meltpools. The cracks penetrated the meltpools regardless of their shape, often propagating through the centre of a meltpool at laser

power 500 W, but no propagation along the meltpool boundaries was observed (Fig. 9b). The crack formation and propagation direction for the DMT mode (Fig. 9c) was more or less independent of the position within the meltpool due to the irregularity of the meltpool shape.

The present study observed that presence of cracks was found to increase with increasing laser power. Figure 10 documents the effect of laser power on total

**Table 4** Results of EDS analysis

Element	450 W				500 W		
	Spot 1	Spot 2	Spot 3	Spot 4	Spot 1	Spot 2	Spot 3
Al	0.3	0.2	0.4	0.0	0.3	6.4	0.0
Si	1.0	1.1	0.4	0.6	0.1	0.4	0.5
Nb	10.8	14.0	3.8	0.3	14.8	1.0	0.0
Mo	5.3	7.7	3.2	1.9	3.4	2.3	3.0
Ti	1.0	0.1	0.9	0.2	1.7	1.1	0.0
Cr	18.8	16.0	19.1	19.1	16.8	17.7	20.3
Mn	1.0	0.3	0.6	0.4	0.2	0.8	1.4
Ni	14.0	13.9	16.7	16.3	45.5	15.5	18.3
Ta	0.5	0.4	0.5	0.4	0.8	0.0	0.0
O	0.0	0.0	0.0	0.0	0.0	7.4	0.0
Fe	Balance	Balance	Balance	Balance	Balance	Balance	Balance

**Figure 11** EDS analysis: **a** laser power 450 W; **b** laser power 500 W.

crack length. The authors Lippold and Xiao [13, 22] mention how important role is played by changes in the AM process (laser power) itself that alter the meltpool size and shape. It is the parameters of the AM process that are often effective in mitigating cracking, because the profile of the meltpool often affects the level of constraints that arise in the final stages of solidification. The latter case provides changes in fluid flow induced by surface tension, which may play a significant role in the final meltpool shape and penetration characteristics. The measured values clearly reflected an increasingly significant effect of the increase in applied laser power, which simply exceeded a certain threshold of the above-mentioned factors, which led to the significant crack formation.

Detailed images of the microstructure with the presence of cellular and dendritic substructures were

taken at interface II near the defects. The microstructure consists of an austenitic matrix with the presence of carbide phases and, in the case of IN718, Laves phases. The results of EDS analyses (Table 4), shown in Fig. 11, for 450 and 500 W laser powers, documented solidification cracks with the presence of Laves phase, carbide phases, and oxide particles. The presence of the above-mentioned precipitates was also reported by other authors [13, 25, 29, 47, 53].

### Grain structure and texture

Electron backscatter diffraction mapping and texture assessment of individual materials (Fig. 4) provided initial information about the individual materials deposited in DMT mode. As can be seen from the IPF maps, coarse-grained 316L stainless steel crystallized

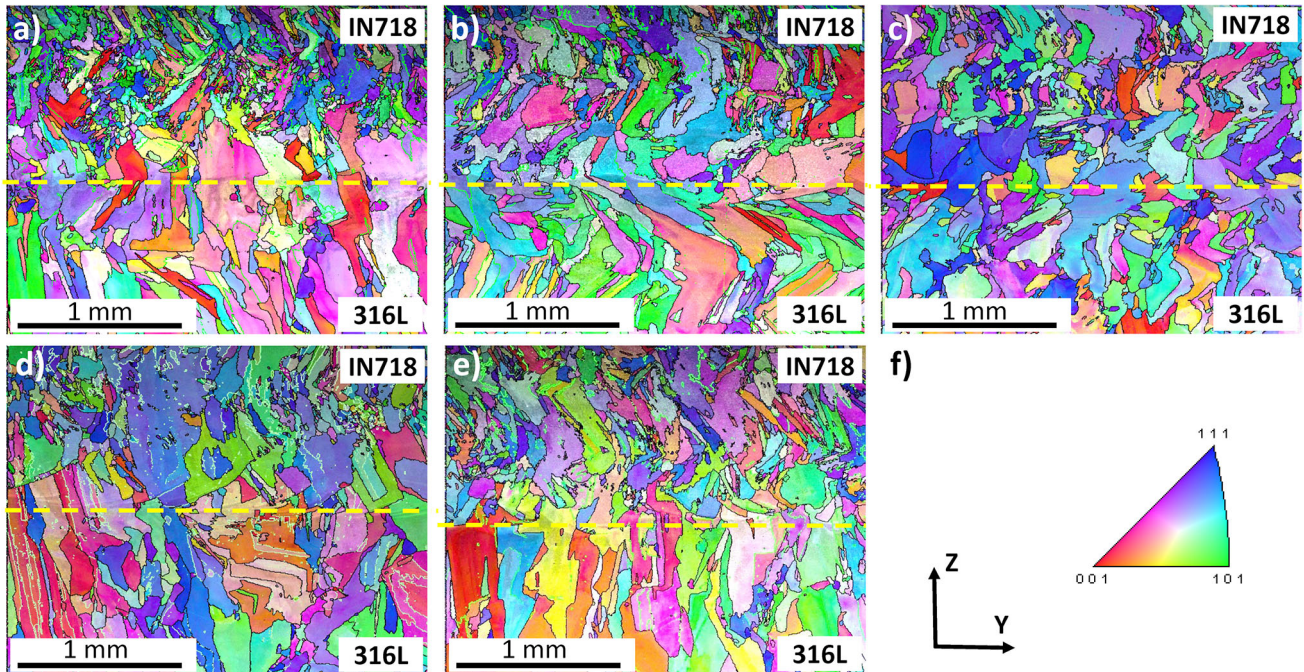


**Figure 12** Inverse pole figure maps at interface I: **a** 350 W; **b** 400 W; **c** 450 W; **d** 500 W; **e** DMT; **f** IPF colour key.

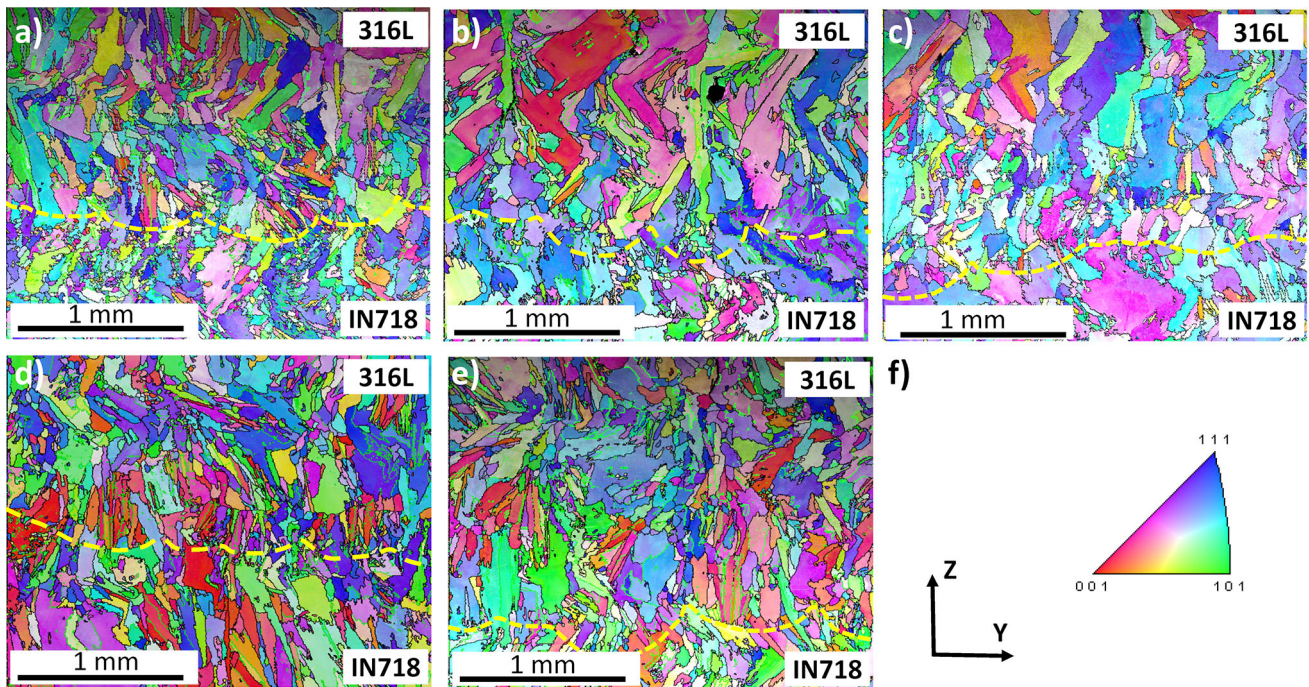


**Figure 13** Inverse pole figure maps at the interface type II: **a** 350 W; **b** 400 W; **c** 450 W; **d** 500 W; **e** DMT; **f** IPF colour key.

with grains extending over several layers, while IN718 crystallized with much finer grains that followed the heat dissipation of the zig-zag deposition strategy. A higher proportion of finer grains with lower texture intensity determined by inverse pole

figures (IN718–2.99; 316L–5.41) may also be influenced to some extent by the number of grains analysed (IN718–885 grains and 316L–472 grains with average diameter  $\geq 35 \mu\text{m}$ ).

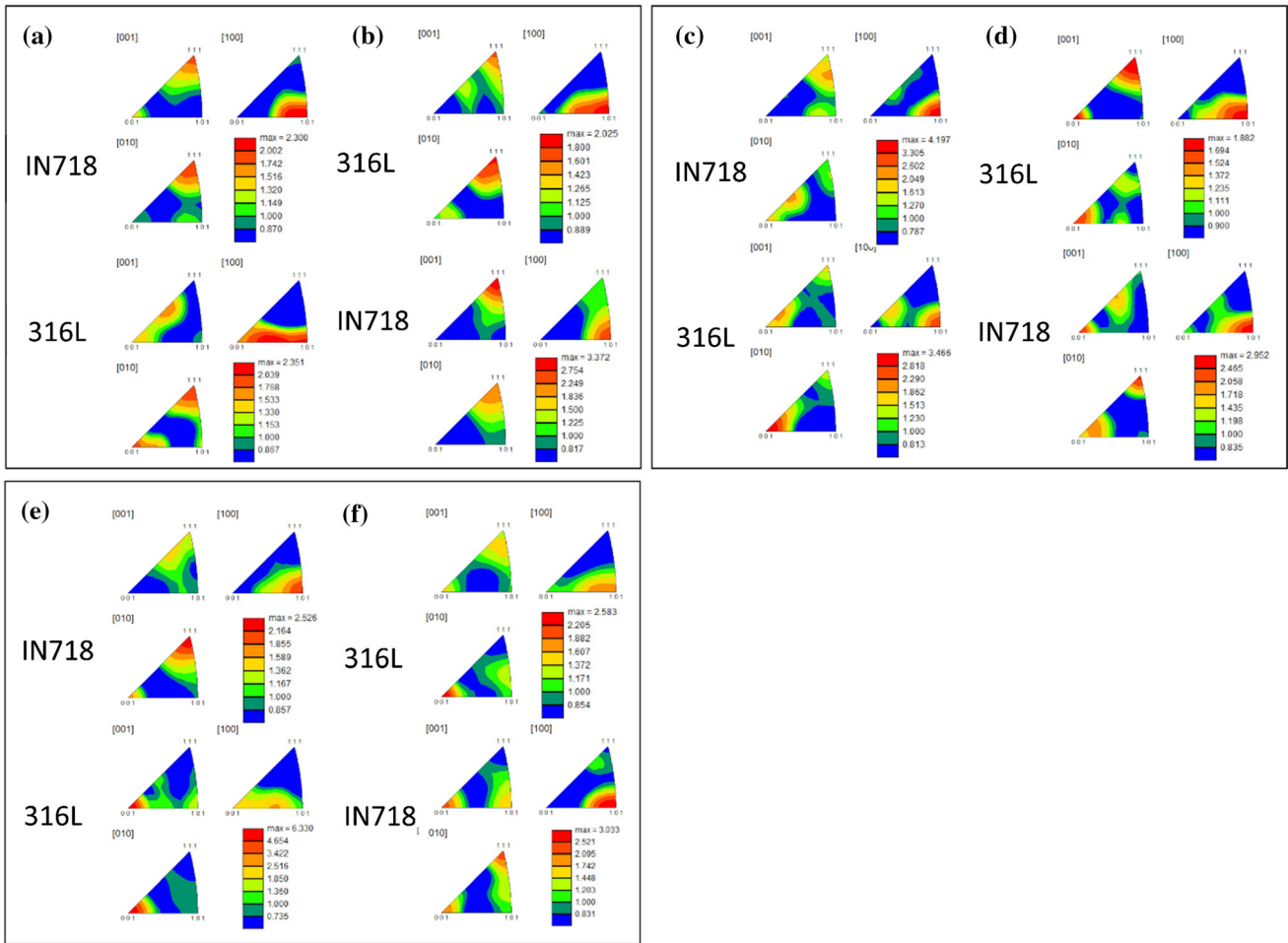


**Figure 14** Inverse pole figures obtained for YZ plane: **a** 350 W-I; **b** 350 W-II; **c** 500 W-I; **d** 500 W-II; **e** DMT-I; **f** DMT-II.

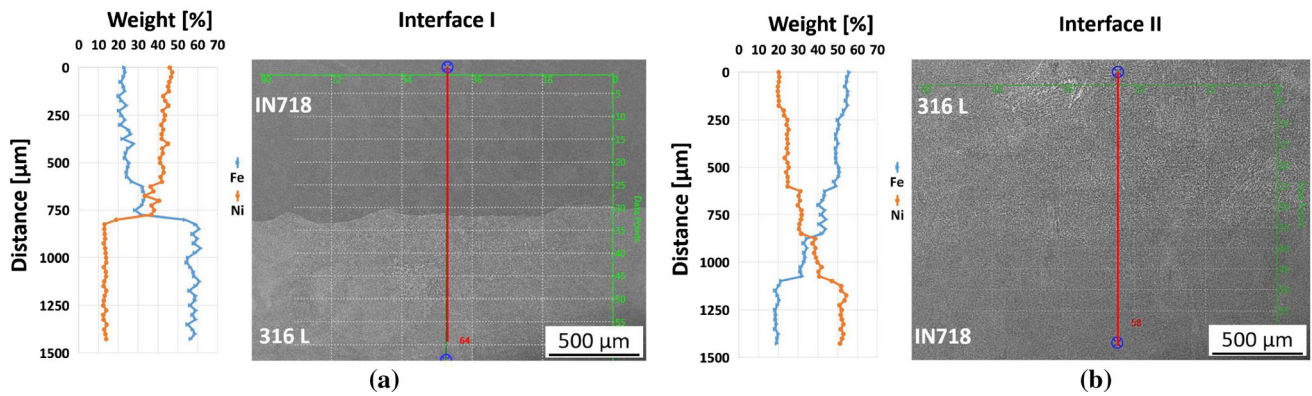
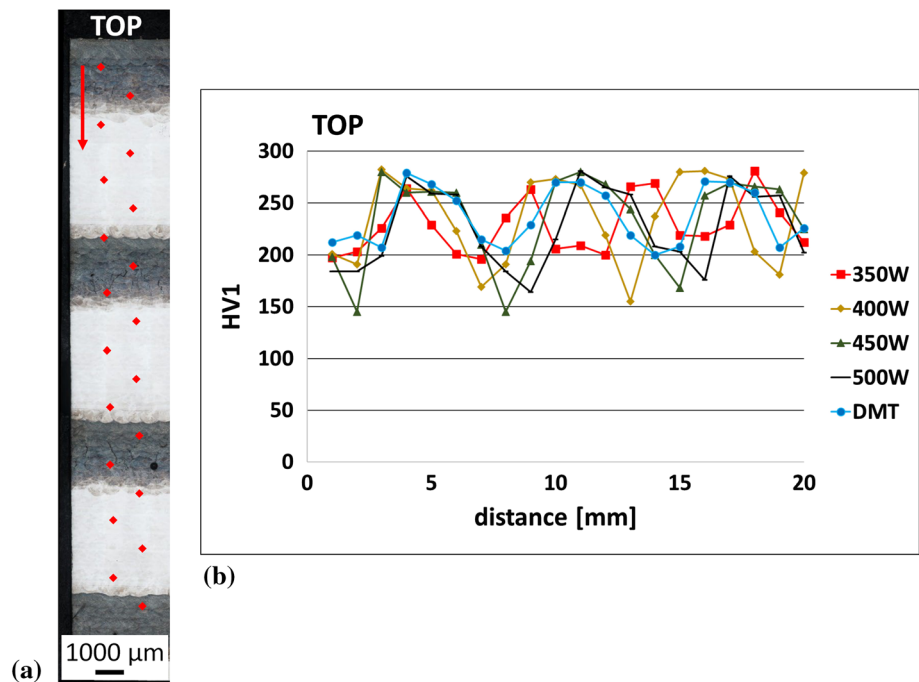


**Figure 15** EDS linescan: **a** interface I; **b** interface II.

Interfaces 2–3 and 3–4 of all the blocks were analysed by EBSD. The IPF maps, representing the type I interface for each applied laser power, capture the nature of the change in the deposited materials from the crystallographic point of view (Fig. 12) and the measured texture intensities. In the first applied

layer, IN718 grains follow both the size and crystal orientation of the original austenitic stainless steel grains. The 500 W laser power increased the texture intensity of the type I interface from 316L to IN718. Thus, it is clear that when the laser power is set to the lowest value, i.e. 350 W, finer and smaller grains

**Figure 16** Hardness measurement through the entire block: **a** testing approach; **b** results of the HV1.



nucleate on the IN718 side. Small grains with almost random orientation crystallized after the application of the second layer of IN718. The DMT mode was largely involved in the formation of elongated grains, which significantly followed the direction of heat dissipation. The 316L steel microstructures were clearly coarser for all applied laser powers, which confirmed the results of individual material deposition using the DMT mode.

In order to capture the very first change in chemical composition, the type II interface starts in the lower third of each IPF map in Fig. 13. EBSD analysis confirmed the LM results, with 316L steel undergoing more remelting than nickel-based alloy with deeper penetration at the interface II. Crystallization of coarser grains appeared already at the first layer's application with the DMT mode, while nucleation of fine grains took place at 350 W.

The inverse pole figures (Fig. 14) obtained for individual interfaces showed the texture intensities of materials deposited with fixed and DMT-applied powers. The EBSD maps over 4 mm<sup>2</sup> achieved statistically meaningful results. The orientation along the three principle crystal planes (001), (101) and (111) were mapped in red, green, and blue, respectively. For most cases, the dominant crystallographic orientation along the build direction was close to [100], which is the dominant crystalline direction in FCC and BCC metals, as solidification growth occurs

preferentially along the cube edge, or  $\langle 100 \rangle$  crystallographic directions. These are sometimes called “easy growth” directions since solidification is most efficient in this orientation according to studies by [11, 13, 57]. Since the type II interface has a gradient change in chemical composition depending on the deposition of each successive layer, the changes in texture intensities do not so markedly affect this type of interface, and no significant change in their difference was observed within the 350 W, 500 W or DMT samples (Fig. 14).

EDS analysis (Fig. 15) confirmed a gradient interface in chemical composition, where with each layer deposited for interface II, there is an increase in mainly Fe content and a decrease in Ni content in the additively manufactured material.

### Mechanical properties

Hardness measurements made at 1-mm intervals along the deposit indicated the variations in hardness present from layer to layer. The hardness profile (Fig. 16) through the entire height of the block, measured from the top towards the platform, captured an interesting trend in the sample created using a power of 350 W. Comparing this profile with other laser powers, the shape of the curve is interesting in terms of the peak values reached. After reaching a peak (hardness of IN718), there is an immediate drop



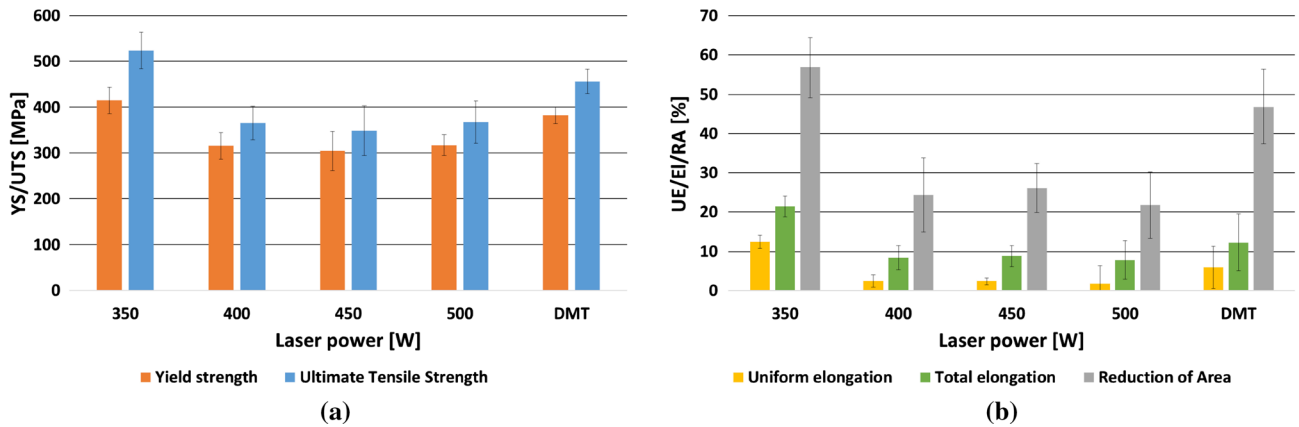


**Figure 17** Miniaturized tensile test results—comparison of blocks: **a** average strength values (YS/UTS); **b** average elongation and reduction in area (UE/EI/RA) values.

**Table 5** Results of the MTT testing of the blocks

Power (W)	YS (MPa)	UTS (MPa)	UE (%)	EI (%)	RA (%)
350	415.0 ± 14.4	523.9 ± 21.3	12.5 ± 2.7	21.4 ± 6.8	56.8 ± 15.7
400	315.9 ± 28.9	365.9 ± 39.4	2.4 ± 1.7	8.4 ± 2.7	24.3 ± 7.7
450	304.7 ± 28.8	348.6 ± 36.8	2.4 ± 1.6	8.8 ± 3.1	26.1 ± 9.4
500	317.1 ± 43.2	367.4 ± 54.8	1.8 ± 0.9	7.8 ± 2.7	21.8 ± 6.3
DMT	382.2 ± 22.5	456.5 ± 46.4	5.9 ± 4.6	12.3 ± 4.9	46.8 ± 8.4

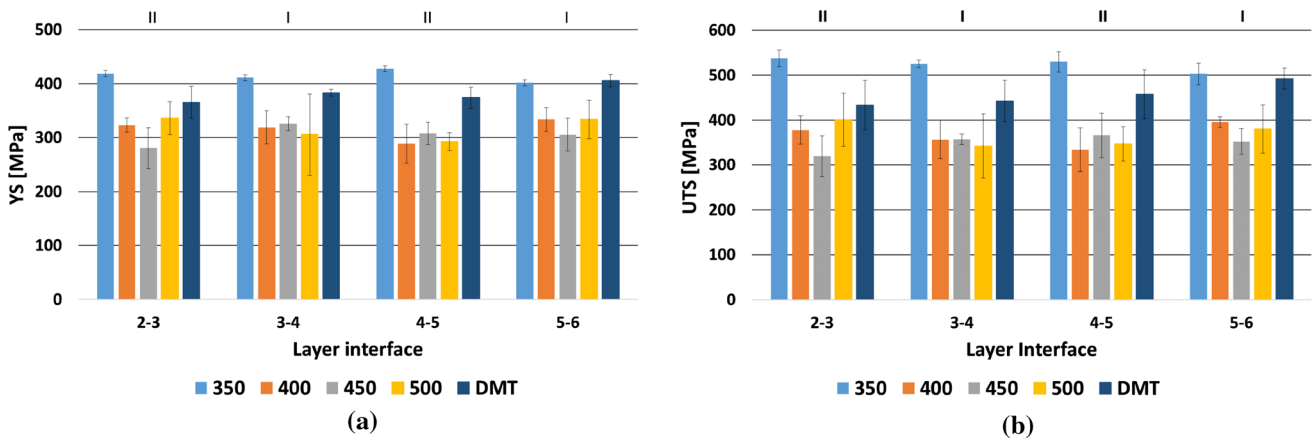


**Figure 18** MTT results—comparison of strength values between individual layer interfaces: **a** YS; **b** UTS.

in hardness values. This profile can be used to assess the characteristics of the interface region between the materials. For the other applied laser powers, the area of the upper maxima (peaks) is wider, i.e. mostly over 3 mm. From this, it can be concluded that the application of higher laser power resulted in a more intense mixing of the materials.

In the study, the tensile properties of the specimens cut from IN718/316L-316L/IN718 interfaces in five

blocks deposited under varying conditions were investigated using miniaturized tensile testing. The comparison of average strength and elongation values as well as the reduction in the cross-sectional area between entire blocks is shown in Fig. 17 and summarized in Table 5.

The block manufactured using 350 W laser power exhibited the highest strength values (415/524 MPa YS/UTS) and was characterized by the highest

**Table 6** Results of the mechanical testing MTT

Laser power (W)	Layer interface	YS (MPa)	UTS (MPa)	UE (%)	EI (%)	RA (%)	Interface type
350	2–3	418.9 ± 13.9	537.8 ± 18.7	11.8 ± 3.7	21.2 ± 6.3	51.5 ± 31.5	II
	<b>3–4</b>	<b>411.3 ± 14.5</b>	<b>525.1 ± 8.2</b>	<b>14.6 ± 1.1</b>	<b>28.0 ± 6.3</b>	<b>59.8 ± 10.4</b>	<b>I</b>
	4–5	428.0 ± 3.0	529.6 ± 22.5	11.7 ± 2.0	17.1 ± 5.6	61.7 ± 10.7	II
	<b>5–6</b>	<b>401.7 ± 12.9</b>	<b>502.9 ± 23.9</b>	<b>11.8 ± 3.6</b>	<b>19.2 ± 6.7</b>	<b>54.2 ± 6.6</b>	<b>I</b>
400	2–3	323.0 ± 13.3	377.6 ± 31.5	2.7 ± 2.6	10.6 ± 1.1	26.3 ± 6.9	II
	<b>3–4</b>	<b>318.9 ± 30.9</b>	<b>356.7 ± 42.7</b>	<b>1.3 ± 0.9</b>	<b>7.2 ± 2.4</b>	<b>21.7 ± 7.7</b>	<b>I</b>
	4–5	288.4 ± 36.0	333.5 ± 48.7	3.2 ± 2.2	9.8 ± 1.8	31.1 ± 7.4	II
	<b>5–6</b>	<b>333.4 ± 22.2</b>	<b>395.6 ± 11.9</b>	<b>2.3 ± 0.5</b>	<b>6.1 ± 2.9</b>	<b>18.2 ± 4.6</b>	<b>I</b>
450	2–3	280.4 ± 38.0	319.1 ± 45.5	1.9 ± 1.1	10.0 ± 1.0	29.0 ± 10.1	II
	<b>3–4</b>	<b>325.9 ± 13.2</b>	<b>357.3 ± 12.0</b>	<b>2.4 ± 2.0</b>	<b>6.8 ± 3.6</b>	<b>28.6 ± 6.5</b>	<b>I</b>
	4–5	307.5 ± 20.8	366.0 ± 50.0	3.4 ± 2.4	9.8 ± 3.9	22.7 ± 9.4	II
	<b>5–6</b>	<b>305.0 ± 30.6</b>	<b>351.9 ± 28.8</b>	<b>2.0 ± 0.8</b>	<b>8.8 ± 3.9</b>	<b>23.9 ± 14.4</b>	<b>I</b>
500	2–3	336.5 ± 30.5	400.8 ± 58.9	2.4 ± 0.8	9.6 ± 3.5	25.7 ± 4.6	II
	<b>3–4</b>	<b>305.8 ± 75.3</b>	<b>342.2 ± 71.7</b>	<b>1.6 ± 1.1</b>	<b>6.6 ± 1.8</b>	<b>25.2 ± 4.8</b>	<b>I</b>
	4–5	292.4 ± 16.5	346.5 ± 38.6	2.0 ± 1.1	9.8 ± 0.5	21.2 ± 2.7	II
	<b>5–6</b>	<b>333.7 ± 35.8</b>	<b>380.0 ± 53.6</b>	<b>1.2 ± 0.3</b>	<b>5.3 ± 1.7</b>	<b>15.0 ± 7.5</b>	<b>I</b>
DMT	2–3	365.6 ± 29.5	433.2 ± 55.5	3.4 ± 2.1	12.3 ± 1.3	52.9 ± 7.0	II
	<b>3–4</b>	<b>383.3 ± 6.5</b>	<b>442.0 ± 46.3</b>	<b>6.6 ± 8.7</b>	<b>12.4 ± 10.9</b>	<b>43.0 ± 14.9</b>	<b>I</b>
	4–5	373.9 ± 19.9	457.8 ± 54.2	5.2 ± 3.0	11.3 ± 2.4	47.5 ± 4.0	II
	<b>5–6</b>	<b>405.8 ± 11.3</b>	<b>492.9 ± 23.2</b>	<b>8.6 ± 2.1</b>	<b>13.1 ± 1.7</b>	<b>43.8 ± 3.0</b>	<b>I</b>

elongation values (higher than 20%). These results were also distinguished by the lowest scatter of recorded values. Different behaviour was observed for the block produced with applied power 500 W, which exhibited the lowest UTS (about 367 MPa) and YS (about 317 MPa) with the lowest elongation values (about 8%). Mechanical properties of individual materials (IN718: YS = 483 ± 5 MPa, UTS = 807 ± 15 MPa, EI = 35 ± 3%; 316L: YS = 338 ± 40 MPa, UTS = 511 ± 37 MPa, EI = 33 ± 8%) are affected by the implementation of functionally graded material interfaces, especially in the case of nickel superalloys.

A graphical summary of the MTT results for the specimens cut from each interface within the same block are presented in Fig. 18. The individual batches of specimens were labelled 2–3, 3–4, 4–5 and 5–6, which are the ordinal numbers of the individual layers through which they pass (Fig. 3b). The Roman numerals I and II in the graph in Fig. 18 and Table 6 indicate the types of individual interfaces. The bolded values of interface I in Table 6 are provided for better orientation in the table.

Generally, the YS and UTS were evaluated in the range from 280 to 428 MPa and from 319 to 537 MPa, respectively, regardless of the interface type. During

the experiment, partial fracturing of the specimens followed by further extension until final rupture was observed. The observations may be related to the accumulated internal defects in the interfaces of single layers (Fig. 20). In the case of Block 350 W, the greatest UTS value was observed for interface 2–3 and the lowest for 5–6. The total elongation varied by a minimum of 17% for all interfaces except 3–4, where a value of almost 30% was reached. In the case of Block 400 W, the average YS values were almost identical for 2–3, 3–4 and 5–6 interfaces, the 2–3 and 5–6 interfaces were distinguished by the highest and the lowest average UTS, respectively. The specimens passing through the second and third layers exhibited the highest average EI (about 11%). A relatively rapid specimen rupture, which was manifested by the lowest EI value, was observed for the 5–6 batch of specimens. In Block 450 W, the lowest strength values and the highest elongation were recorded for the specimens originated from the 2–3 interface. The specimens from the 3–4 interface batch behaved in the opposite manner, nevertheless, both groups exhibited comparable reductions of cross-sectional area (RA). The specimens extracted from the 4–5 and 5–6 interfaces showed almost identical strength and

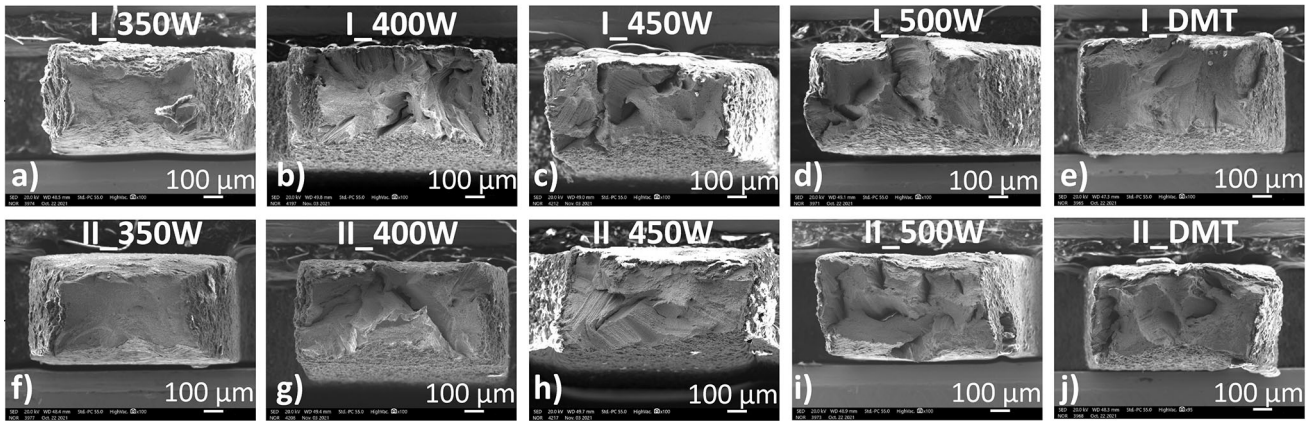


**Figure 19** Overview images of the fracture surfaces of the samples at type I (top row: a–e) and type II (bottom row: f–j) interfaces.

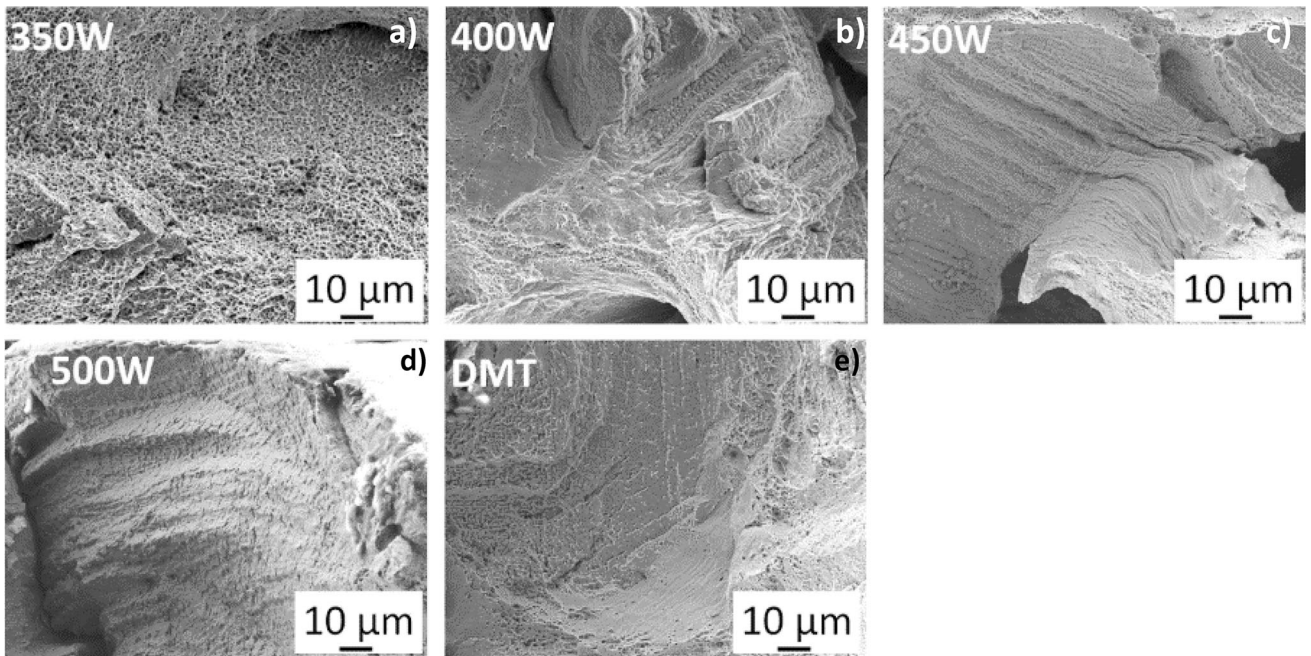


**Figure 20** Applied laser power: **a** 350 W—transcrystalline ductile fracture with dimple morphology; **b** 400 W—ductile fracture with dimple morphology combined with SC; **c** 450 W—DDC with SC; **d** 500 W—SC; **e** DMT—SC combined with dimpled morphology ductile fracture.

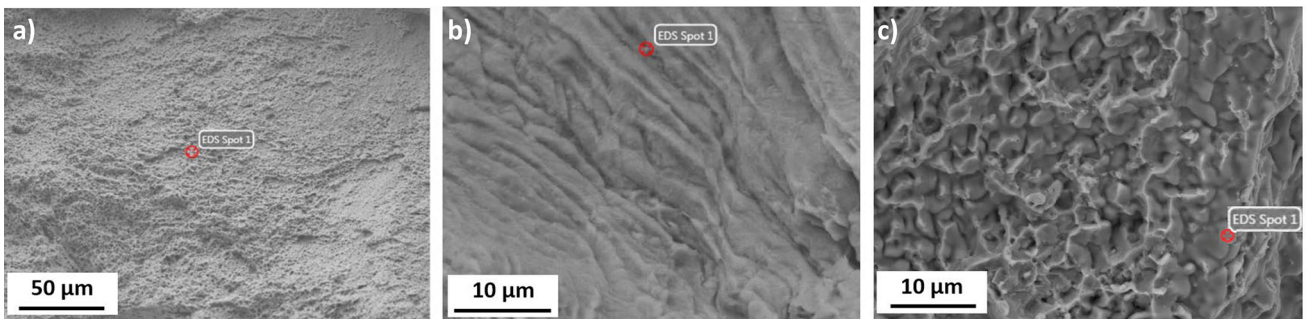


**Figure 21** EDS analysis of the fracture surface: **a** transcrystalline ductile fracture—power 350 W; **b** ductility dip cracking area—power 450 W; **c** solidification cracking–DMT.

**Table 7** Results of the EDS analysis

Element	Laser power (W)		
	350	450	DMT
Weight %			
O		10.8	
Al		1.5	0.5
Si	5.8	1.1	0.6
Nb	1.2	1.0	3.0
Mo	3.1	3.1	3.4
Cr	19.3	15.8	20.8
Ni	12.2	11.5	18.5
Fe	Balance	Balance	Balance

RA values; however, the EI of the 5–6 batch was slightly lower. The specimens from the 2–3 and 5–6 interfaces of Block 500 W yielded the highest strength values, where the EI values were about 10% for the 2–3 interface batch and almost half for 5–6. The average YS and UTS for 3–4 and 4–5 was similar; however, the values obtained for the 3–4 batch were highly scattered. Block 500 W exhibited the highest scatter of strength values. In the case of the DMT block, interface 5–6 reached the highest values of strength and uniform elongation. However, the total elongation was similar for all interfaces within this block. Interface 2–3 was characterized by the poorest overall mechanical performance, manifested by the lowest strength and uniform elongation values. This interface was also distinguished by the highest RA.

Considering the comparison of tensile characteristics between interfaces within the same blocks, it is worth noting that in each case, the results are characterized by a relatively low repeatability, so there is also high standard deviation. The results of the mechanical testing proved the increasing power and the associated increased occurrence of defects, which significantly affect the individual interfaces, causes the differences in mechanical property values between the individual interfaces to be eliminated.

### Fractographic analysis

Fractographic analysis was performed on interfaces 2–3 and 3–4. These samples were then prepared for detailed EBSD analysis. The fracture surfaces fully reflect the results obtained from the MTT tests and metallographic analyses (Fig. 19), i.e. the minimal

presence of cracks in the material at 350 W did not detrimentally affect material failure.

The fracture surface at 350 W with both types of interfaces showed ductile transcrystalline failure with the presence of dimples. At higher powers, solidification cracking and ductility dip cracking were present on the fracture surfaces, which contributed significantly to the reduction in the measured values, especially ultimate tensile strength (UTS) and yield strength (YS). The fracture surface of solidification cracking tend to show a cellular or dendritic morphology and is usually associated with liquid films along SGBs [13]. Solidification cracking and ductility dip cracking propagated along grain boundaries, i.e. mainly via intergranular propagation. Outside the areas of detected cracks, the failure mechanism of the material was ductile with typical dimpled morphology. Examples of detailed images of the fracture surfaces with typical fractographic features are shown in Fig. 20. Despite the rapid solidification process, the interface was not free of segregation.

EDS analyses were performed on fracture surfaces to confirm the location of the fracture surface at each 316L/IN718 material interface (Fig. 21, Table 7). The local chemical analyses confirmed that failure of the 316L/IN718 functionally graded materials always occurred on the 316L stainless steel side. If solidification cracks or ductility dip cracks were present on the fracture surface, the presence of oxygen was detected, demonstrating that the cracks were oxidized during the additive manufacturing process. This is indicated by the shape and character of the defect (Fig. 21b, c), which has fractographic features of ductility dip cracks with microscopic wavy appearance and SC with an “eggcrate”-type appearance [13].

### Discussion

An attempt of conventional welding methods to weld crack-free nickel-based super alloy IN718 and austenitic stainless steel 316L using tungsten arc welding process has been successfully investigated by employing the filler metals [21]. The great potential of powder-based DED technology compared to conventional welding methods lies mainly in the lower heat input, residual stresses, warpage and distortion and in the higher accuracy of deposited material combined with significant cost and time savings and

can be used for applications with dissimilar material compositions [1–8].

Functionally graded materials (316L–IN718) were successfully deposited via powder-based DED with different laser power values ranging from 350 to 500 W with step of 50 W including innovative DMT mode and subjected to detailed analysis of microstructure and mechanical properties. The present study explored certain limitations resulting from the AM of the FGM materials. Metallographic analysis monitored the effects of changing the process parameters, namely the laser power, on the resulting microstructure. FGM materials showed the presence of inhomogeneous grain morphologies, which were dependant on the applied power, but are also related to the coefficient of thermal expansion of individual materials [19, 50].

In the present study, two types of interfaces were explored. Type I, detected at the 316L stainless steel to IN 718 interface, depicted a shallower penetration than the type-II at the IN718 to 316L stainless steel interface. Interface I (Fig. 6) exhibited planar, cellular and dendritic growth modes, while planar growth at interface II was not confirmed by metallographic analysis as material 316L undergoes more remelting than nickel-based alloy at the interface II (Fig. 5). This difference can be explained by the lower energy absorption rate and lower thermal conductivity of IN718 relative to 316L [16, 22]. The intense fluid flow in the meltpool and the temperature gradient along the fusion boundary had an effect on the formation of UMZ (Fig. 8). Either 316L or IN718 was observed to mix into the weld metal at both interfaces.

Good metallurgical bonding was obtained at the interface I (Fig. 6), when austenitic stainless steel transitions to nickel superalloy as has been already investigated in recent works [14, 16, 22, 23, 27, 51, 56]. Detailed metallographic analysis detected the presence of defects in the second type of interface (Fig. 9), i.e. when 316L stainless steel was applied on IN718. The formation of undesirable defects and microstructural inhomogeneity was caused by complex and variable thermal history [50]. Metallographic analyses explored defects in the form of solidification cracking (SC) and ductility dip cracking (DDC) with the presence of the Laves phases, oxides and carbides. As has been reported in recent studies [13, 20, 25, 29, 47, 53], the strain localization in materials with FCC lattice gives rise to grain boundary sliding and preferential void formation

and cracking at the grain boundaries. Stainless steels and nickel superalloys are generally susceptible to these crack mechanisms during welding and additive manufacturing. These defects were not observed when the order of application of the alloys was reversed.

The mechanism of crack formation in the present study can be attributed to several factors such as natural shrinkage, thermal and residual stresses, the incidence of liquid films and the meltpool size and shape [13, 18, 22]. The latter case may provide changes in fluid flow induced by surface tension, which may play a significant role in the final meltpool shape and penetration characteristics as studied by Chen and Xiao [16, 22]. Their results of simulations of the direction of flow of liquid metal within the meltpool for each interface type showed that surface tension is considered to be the primary driving force of convection flow. In particular, 316L has a relatively higher laser absorption rate and higher thermal conductivity, but lower viscosity than IN625. The aforementioned influence of flow on the quality of functionally graded materials at interface II can be further enhanced by the amount of applied power.

Due to the different temperature intervals of the solidus and liquidus of the steel and nickel alloys (316L: 1375–1440 °C and IN718: 1290–1350 °C), the subsequent application of steel to Inconel resulted in its partial melting, which matched well the findings of Melzer et al. [14]. The changing laser power affects the deposition process, and meltpools with a more regular shape and more stable height were formed at fixed powers than in the case of the DMT mode (Fig. 7), when irregular melting of individual layers and formation of irregular shapes of individual meltpools occurred. This change was observed most strongly for interface II, while interface I did not show this phenomenon significantly. Higher power, i.e. 500 W, caused a greater remelted depth of the material due to the higher energy input and the associated increased size of the meltpools. These observations confirmed the results of [12, 25] that the size and shape of the meltpool is mainly related to the laser power and scanning speed, which provides a good model for the characteristics of meltpools. The effect of energy input on interface evolution (Figs. 12 and 13) as the laser power and the associated energy density changes, and the change in sizes and shapes

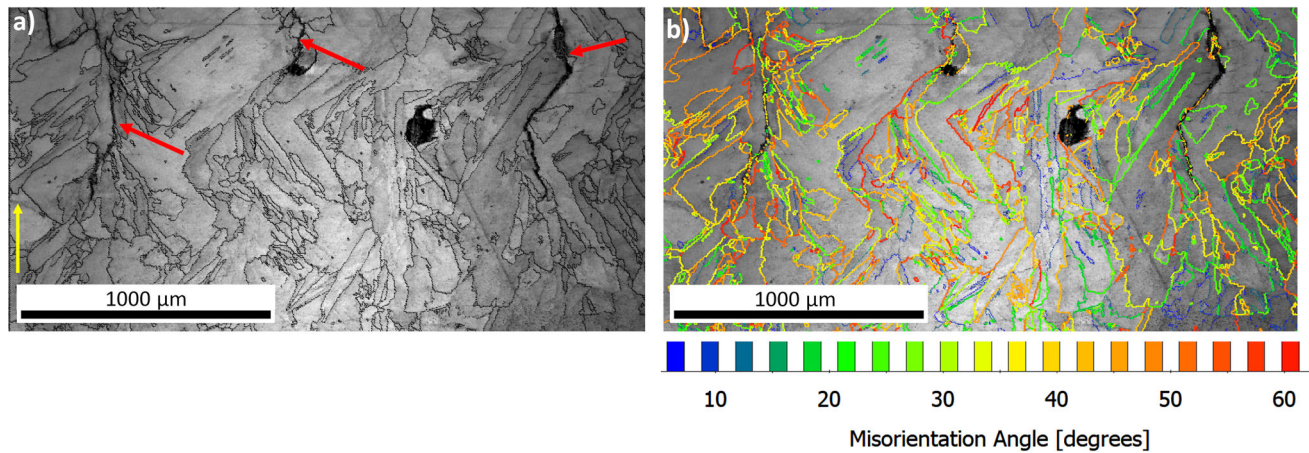


**Figure 22** OIM software post-processing interface II: **a** Image quality (IQ) map; **b** IQ with highlighted grain boundaries misorientation angles. Yellow arrow indicates the building direction (Z).

of meltpools matched well with the findings in [12, 54, 55].

Crack propagation occurred along grain boundaries, with crack lengths exceeding the height of several layers. In the present study the cracks penetrated the meltpools independently of their shape. Propagation was often observed through the centre of the meltpool with an applied laser power of 500 W, but no propagation occurred along the meltpool boundaries. At a laser power of 350 W, small cracks at interface II were detected from layer 2 onwards. These are really fine cracks without massive propagation, exceeding at most two layers, directed to the centre of the shallow meltpool. The crack formation and propagation direction for the DMT mode was more or less independent of the position within the meltpool due to the irregularity of the meltpool shape.

The IPF maps, representing interfaces I and II of each applied laser power, captured the nature of the

change in the deposited materials from the crystallographic point of view (Figs. 12, 13) and the measured texture intensities (Fig. 15). Grain crystallization initiated by epitaxial nucleation followed by the mechanism of grains' competitive growth, formed grains that retained the same crystallographic orientation as the grains of the initial base metal as referred to Smith, Yan and Lippold [13, 23, 24]. EBSD data post-processing in OIM software (Fig. 22) revealed that the cracks formed at the interface II, i.e. where 316L stainless steel is deposited on a substrate of IN718, were found to be distributed along HAGB with angles in the interval 30°–50°. Cracks are highlighted with red arrows and with colour indication of misorientation angles. This is in agreement with [13, 19] because SC and DDC cracks always propagate along the high-angle grain boundaries (HAGBs) with crystallographic misorientation angles > 15°. The cracks were

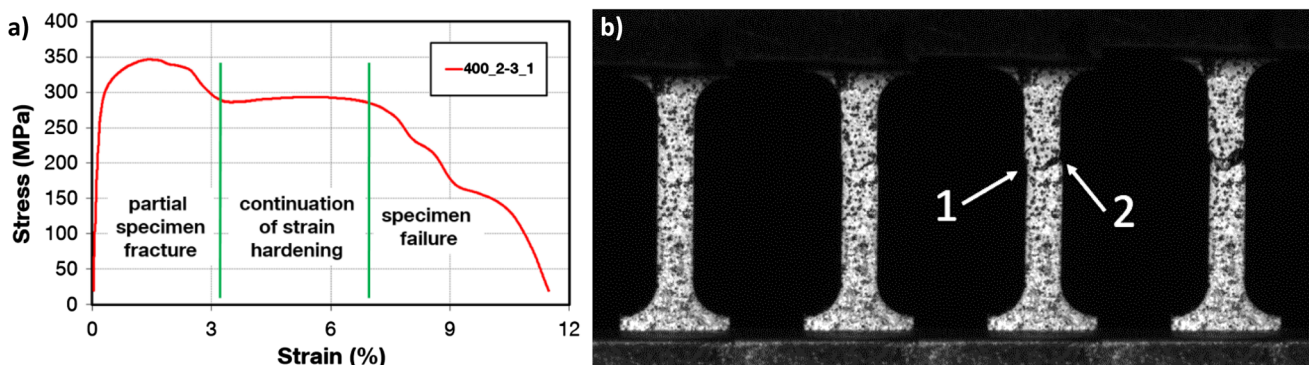


**Figure 23** Block 400 W, interface 2–3: **a** Stress–strain curve example; **b** specimen deformation sequence, where “1” is a continuous material with remaining plasticity and “2” is a partial material failure as a result of local defects.

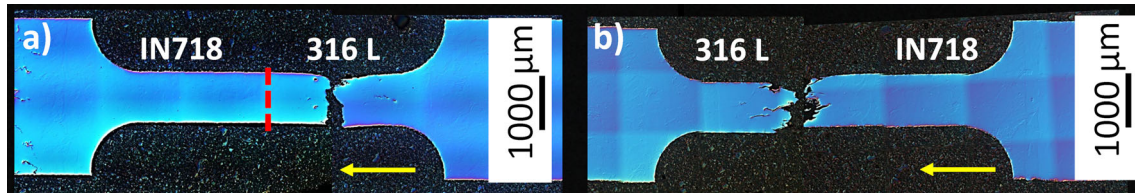


**Figure 24** Metallographic sections of MTT samples after testing: **a** interface I; **b** interface II. Yellow arrow indicates the building direction (Z).

intercrystalline rather than transcrystalline. This finding shows agreement with Han [30].

The cumulative results of all specimens from the individual blocks (Fig. 17) exhibited comparable strength values. The tensile properties of the individual material layers were consistent across the deposited height for both 316L and IN718. The differences between average strength values of the specimens cut from different layers lay within their standard deviation ranges so any dependence of the tensile characteristics on the extraction layer was not observed. The highest strength and elongation values were recorded for Block 350 W. In contrast, the specimens cut from Block 500 W exhibited significantly worse mechanical performance in terms of strength and elongation. These specimens were also characterized by the highest scatter of the values, which expresses increased uncertainty of measured data. This phenomenon correlates with the length of solidification crack observed by means of LM. The specimens from Block 350 and 500 W showed the lowest and the highest values of the crack length, respectively. Therefore, in this case the high amount of defects exceeding critical dimensions can be one of the reasons of high scatter of values and decreased quality of the component. During the experiment, a partial fracture of the specimens followed by their further extension until final rupture was observed. This influenced the appearance of the stress–strain curves, where division into several steps was observed (Fig. 23a). The observations may be related to the accumulated internal defects in the interfaces of single layers and were noticed for most of the specimens in each block, regardless of the interface type [58, 59]. The MTT specimen sequence during testing at different levels of extension is shown in Fig. 23b. In tensile test specimens, a stress concentration appears after onset of plastic instability (necking), where a complex stress state has to be considered. As a consequence of localized deformation, a stress concentration occurs in the region of the

accumulated dislocations as well as the creation of voids, their coalescence and finally specimen failure. In this study, the miniaturized tensile specimens have the defects that induce a stress concentration before onset of plastic instability is reached. In these locations, a partial material failure occurred; nevertheless, the remaining specimen cross-sectional area still underwent a strain hardening since residual plasticity was not fully exhausted.

The fracture pattern of the lowest applied power (350 W) is indicative of a high-energy ductile fracture with a dimpled morphology (Fig. 20a). The shape of the fracture surface also shows relatively pronounced contraction, indicating good plasticity of the samples (measured ductility is about 21%). Figure 24 captured metallographic sections of MTT samples after testing. Material failure occurred for all samples at both interfaces in the 316L material region. For interface I (from 316L to IN718), the sharp interface type I (red dashed line) was defect-free, but the influence on the micromechanical test results was due to the presence of solidification cracks from the previous interface (Fig. 24a). Fracture localization at interface II, i.e. the gradient interface (type II) from IN718 to 316L was observed directly at the interface (Fig. 24b). The yellow arrows in the figures indicate the building direction of the material. The results of the present study are not fully consistent with other works by Li et al. [27], where the microstructure and mechanical properties of functionally bimetallic Inconel steel materials were similar for interface type I (from 316L stainless steel to IN 718). However, Li did not report the presence of defects that would reduce the mechanical properties of interface type II, which were also present in the specimens and significantly affected the results of the tensile testing in the present study. This difference may be attributed to the use of thermal milling prior to applying the second material in Li's research.

Fractographic analysis revealed that the solidification or ductility dip cracks present on the fracture

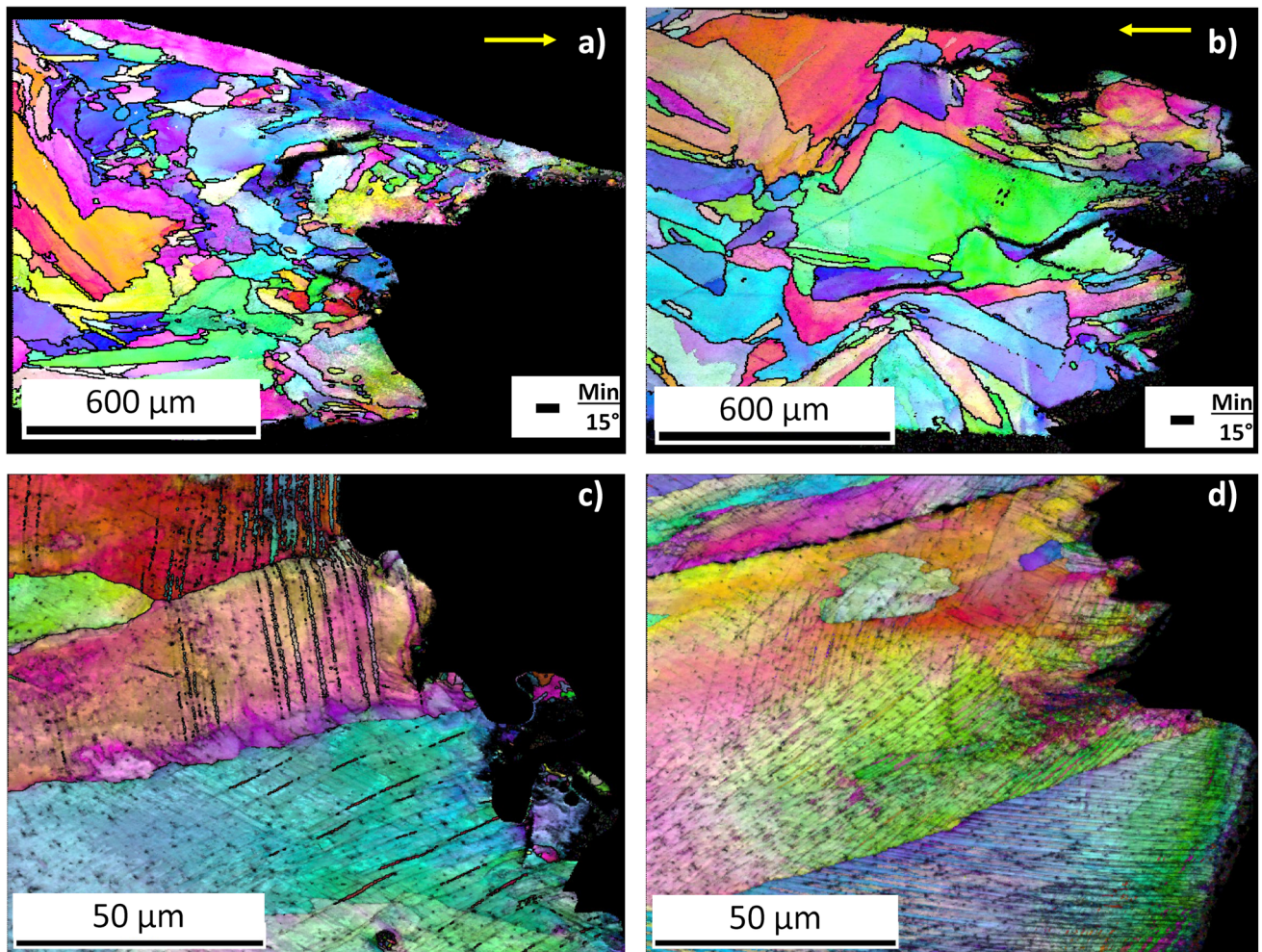


**Figure 25** MTT specimens IPF maps: **a** DMT-I; **b** 400 W-II; **c** detail DMT-I; **d** detail 400 W-II. Yellow arrow indicates the building direction (Z). Yellow arrow indicates the building direction (Z).

surfaces of several MTT samples were oxidized, most likely during the additive manufacturing process. The presence of oxygen in the powder-based DED process should be minimized using argon as a shielding gas. The presence of oxygen (Fig. 21b) has also been observed and reported by Smith et al. [23], as the elevated temperatures during DED allow the decomposition of oxide compounds from gas atomized powder and their dissolution in the molten pool. With a gradual decrease in temperature, reoxidation and oxide nucleation and growth arise.

EBSD analysis also obtained an integral characterization of the material as well as information about the orientation of individual grains in the microstructure, their size and their relative rotation and deformation. These characteristics were also applied to the analysis of MTT samples oriented parallel to the printing direction (produced by

WEDM and tested in the YZ plane). Figures 25 and 26 show the IPF and Grain Reference Orientation Deviation (GROD) maps, which show the distribution of local misorientation within a grain. The figures show the most interesting examples in terms of crack propagation and strain distribution within individual grains near the fracture surface of the MTT samples.

Near-fracture cracks propagation (Fig. 25a, b) occurred mainly intergranularly along high-angle boundaries with misorientation angles  $> 15^\circ$ , which was determined by the EBSD post-processing in OIM software. More pronounced material deformation in the immediate vicinity of the fracture, which always took place in 316L stainless steel, was noticed in the presence of slip bands (Fig. 25c, d).

The Grain Reference Orientation Deviation (GROD) maps in Fig. 26 with colour identification of



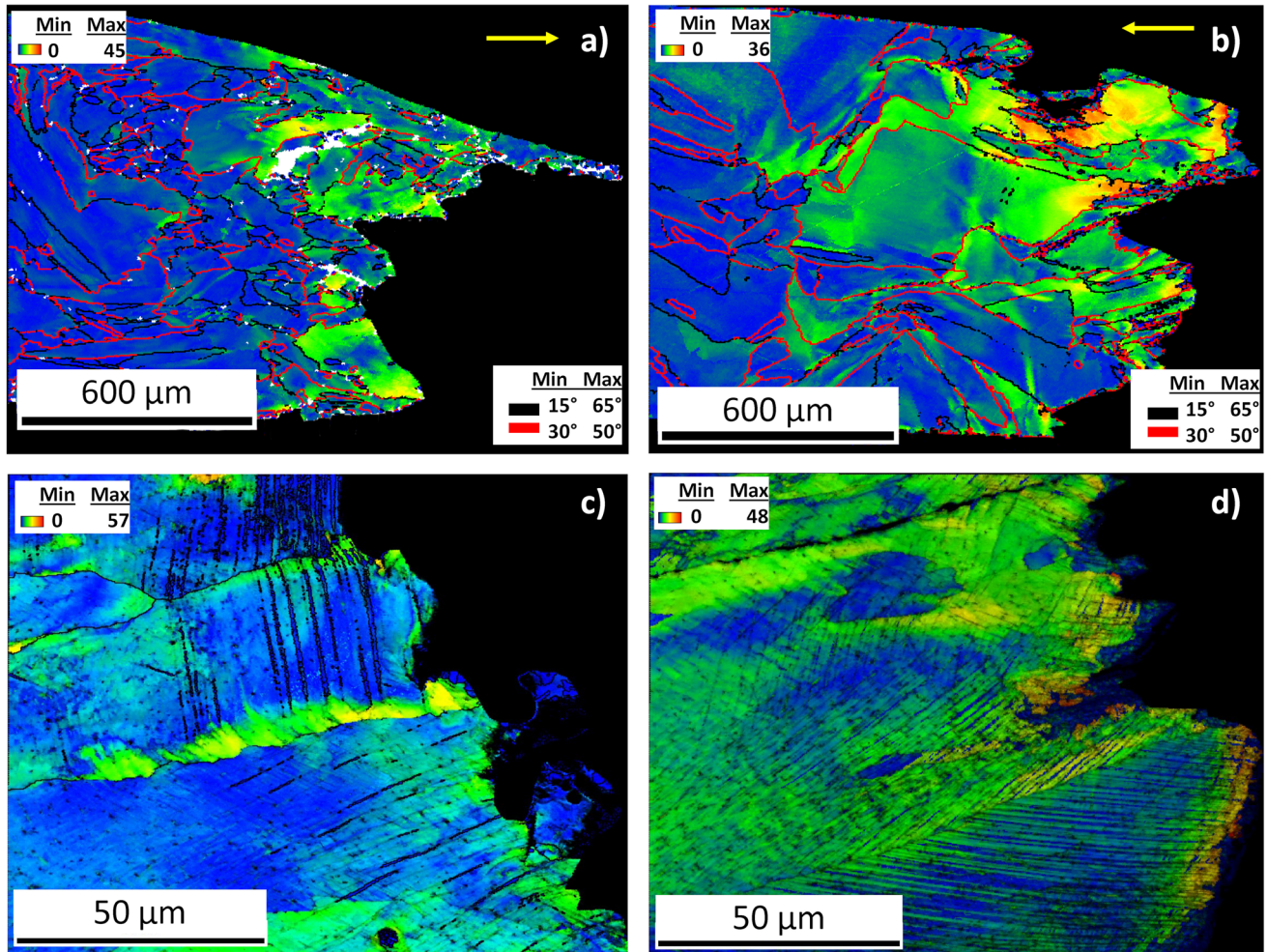


**Figure 26** MTT specimens GROD: a DMT-I; b 400 W-II; c detail DMT-I; d detail 400 W-II. Yellow arrow indicates the building direction (Z).

HAGBs with intervals  $15^{\circ}$ – $65^{\circ}$  (black) and  $30^{\circ}$ – $50^{\circ}$  (red) showed the distribution of local misorientation within a grain. Colour coherency in GROD angle maps, which is linked to the local deformation conditions, proved that certain grains are segmentally deformed with higher levels of lattice misorientation towards the fracture surfaces, where the cracks are initiated.

The best mechanical property results in the present study were achieved with the laser power 350 W. The tensile properties of the 316L–IN718 (Type I) and IN718–316L (Type II) interfaces, tested at room temperature by specialized miniature tests in ZYX orientation, reached values in the range of mechanical properties of pure materials. In general, experimentally measured values of YS and UTS in the range of 280–428 and 319–537 MPa, respectively, were evaluated for individual blocks deposited in DMT mode

and laser power range 350–500 W regardless of the interface type. The outcomes achieved for the optimized laser power, namely 350 W, reached better results compared to the published work of Yang et al. [28], in which a type II interface was studied (i.e. change from IN718 to 316L stainless steel).

The study [24] also confirmed the location of the fracture in the 316L region, which is in full agreement with the results of the present study. The experimental program of this study was aimed at optimizing the laser power of powder-based DED on the quality of individual interfaces of deposited materials. Both in terms of microstructure and interface quality and in terms of mechanical properties, the optimum laser power was found to be 350 W for these types of functionally graded materials for both types of interfaces.

## Conclusions

Application of functionally graded materials 316L/IN718 deposited by powder-based directed energy deposition was the main scope of the present research study. The order of application of stainless steel on nickel superalloy and vice versa generated two different types of interfaces that significantly affected the overall quality of the deposited component. Optimization of the laser power of powder-based directed energy deposition in terms of the microstructure evolution, interface quality and mechanical properties was achieved, and the following conclusions are summarized:

- Inhomogeneous grain morphologies of both materials at individual interfaces correlated to the complex thermal history of the deposited material.
- The application of direct metal tooling mode and comparison of the properties with the builds deposited with constant laser parameters brought novelty aspect to the research of the functionally graded materials.
- Miniaturized tensile tests at the individual interfaces' types throughout the deposit did not prove any dependence of the tensile characteristics on the sample position, but were strongly associated with changes in deposition parameters, namely the laser power.
- The grain boundaries were a critical element in the successful application of stainless steel on nickel superalloy in a horizontal configuration, while the crack-free interface, regardless of the applied power at interface I (IN718 applied on 316L), demonstrated the promising application of these functionally graded materials with the possibility of successful production by powder-based directed energy deposition.
- In the case of the application of 316L stainless steel on nickel superalloy IN718, the main cause of the reduced values of the mechanical properties was the formation of solidification cracks together with ductility dip cracking, which tend to increase in frequency as applied power is increased.
- The presence of cracks at the II interface is attributed to the sequence of the deposited materials, their different melting temperatures, coefficient of thermal expansion and especially applied laser power, which affected the shape and size of

the melt pools and the associated different residual stresses.

- The fracture site for both types of interfaces was always in the region where 316L prevails.
- The results of the present study proved that in terms of interface quality and mechanical properties, a laser power of 350 W was found to be optimal for this type of functionally graded material for both types of interfaces.
- The research presented good metallurgical bonding achieved by powder-based directed energy deposition technology with a promising application of nickel superalloy Inconel 718 deposition on a 316L stainless steel substrate in a horizontal configuration.

## Acknowledgements

The paper was developed with the support from the ERDF project Pre-Application Research of Functionally Graded Materials by Additive Technologies, No. CZ.02.1.01/0.0/0.0/17\_048/0007350.

## Author Contributions

MK involved in conceptualization, investigation and writing—original draft. TS involved in investigation and review and editing. SR involved in investigation and writing—review and editing. MB involve in investigation. JD involved in supervision, funding and review and editing.

## Declarations

**Conflict of interest** The authors declare no conflict of interest.

## References

- [1] Piscopo G, Iuliano L (2022) Current research and industrial application of laser powder directed energy deposition. *Int J Adv Manuf Technol*. <https://doi.org/10.1007/s00170-021-08596-w>
- [2] InssTek (2022) [http://www.insstek.com/content/am\\_module](http://www.insstek.com/content/am_module). Accessed 31st May 2022
- [3] Uhlmann E, Düchting J, Petrat T et al (2021) Effects on the distortion of Inconel 718 components along a hybrid laser-based additive manufacturing process chain using laser

- powder bed fusion and laser metal deposition. *Prog Addit Manuf* 6:385–394. <https://doi.org/10.1007/s40964-021-00171-9>
- [4] Graf B, Schuch M, Kersting R, Gumenyuk A, Rethmeier M (2015) Additive process chain using selective laser melting and laser metal deposition. In *Lasers in Manufacturing Conference*.
- [5] Azarniya A et al (2019) Additive manufacturing of Ti-6Al-4V parts through laser metal deposition (LMD): process, microstructure, and mechanical properties. *J Alloys Com* 804:163–191. <https://doi.org/10.1016/j.jallcom.2019.04.255>
- [6] Kok Y, Tan XP, Wang P, Nai MLS, Loh NH, Liu E, Tor SB (2018) Anisotropy and heterogeneity of microstructure and mechanical properties in metal additive manufacturing: a critical review. *J Mat Des* 139:565–586. <https://doi.org/10.1016/j.matdes.2017.11.021>
- [7] Lin PY, Shen FC, Wu KT, Hwang SJ, Lee HH (2020) Process optimization for directed energy deposition of SS316L components. *J Ad Man Tech* 111:1387–1400. <https://doi.org/10.1007/s00170-020-06113-z>
- [8] Kim JS, Kang BJ, Lee SW (2019) An experimental study on microstructural characteristics and mechanical properties of stainless-steel 316L parts using directed energy deposition (DED) process. *J Mech Sci Tech* 33(12):5731–5737. <https://doi.org/10.1007/s12206-019-1116-1>
- [9] Gibson I, Rosen D, Stucker B (2015) *Additive manufacturing technologies*, 2nd edn. Springer Science Business Media, New York
- [10] Wei C, Li L, Zhang X, Chueh Y (2018) 3D printing of multiple metallic materials via modified selective laser melting. *CIRP Ann Man Tech* 67:245–248. <https://doi.org/10.1016/j.cirp.2018.04.096>
- [11] Chen Y, Zhang K, Huang J, Hosseini SRE, Li Z (2016) Characterization of heat affected zone liquation cracking in laser additive manufacturing of Inconel 718. *J Mat Des* 90:586–594. <https://doi.org/10.1016/j.matdes.2015.10.155>
- [12] Hallberg E (2018) Investigation of hot cracking in additive manufactured nickel-base superalloys. Process optimization and crack removal with hot isostatic pressing. Master Thesis, Chalmers University of Technology.
- [13] Lippold JC (2015) *Welding metallurgy and weldability*. Wiley, Hoboken, New Jersey
- [14] Melzer D, Džugan J, Koukolíková M, Rzepa S, Vavřík J (2021) Structural integrity and mechanical properties of the functionally graded material based on 316L/IN718 processed by DED technology. *J Mater Sci and Eng A* 811:141038. <https://doi.org/10.1016/j.msea.2021.141038>
- [15] Fajobi MA, Loto TR, Oluwole OO (2021) Austenitic 316L stainless steel; corrosion and organic inhibitor: a review. *KEM* 886:126–132. <https://doi.org/10.4028/www.scientific.net/kem.886.126>
- [16] Chen N, Khan HA, Wan Z, Lippert J, Sun H, Shang S-L, Liu Z-K, Li J (2020) Microstructural characteristics and crack formation in additively manufactured bimetal material of 316L stainless steel and Inconel 625. *Add Manuf* 32:101037. <https://doi.org/10.1016/j.addma.2020.101037>
- [17] Akca E, Gursel A A (2015) Review on superalloys and IN718 nickel-based INCONEL superalloy. *Per Eng Nat Sci* 3 No. 1. <https://doi.org/10.21533/pen.v3i1.43.g47>
- [18] Hinojos A, Mireles J, Reichardt A, Frigola P, Hosemann P, Murr LE, Wicker RB (2016) Joining of Inconel 718 and 316 stainless steel using electron beam melting additive manufacturing technology. *Mater Des* 94:17–27. <https://doi.org/10.1016/j.matdes.2016.01.041>
- [19] Mohd Yusuf S, Zhao X, Yang S, Gao N (2021) Interfacial characterisation of multi-material 316L stainless steel/Inconel 718 fabricated by laser powder bed fusion. *Mat Lett* 284(1):128928. <https://doi.org/10.1016/j.matlet.2020.128928>
- [20] Qiu Ch, Chen H, Liu Q, Yue S, Wang H (2019) On the solidification behaviour and cracking origin of a nickel-based superalloy during selective laser melting. *Mat Char* 148: 330–344, ISSN 1044-5803. <https://doi.org/10.1016/j.matchar.2018.12.032>
- [21] Ramkumar KD, Patel SD, Praveen SS, Choudhury DJ, Prabakaran P, Arivazhagan N, Xavier MA (2014) Influence of filler metals and welding techniques on the structure–property relationships of Inconel 718 and AISI 316L dissimilar weldments. *Mater Des* 1980–2015(62):175–188. <https://doi.org/10.1016/j.matdes.2014.05.019>
- [22] Xiao Y, Wan Z, Liu P, Wang Z, Li J, Chen L (2022) Quantitative simulations of grain nucleation and growth at additively manufactured bimetallic interfaces of SS316L and IN625. *J Mater Process Technol* 117506. <https://doi.org/10.1016/j.jmatprotec.2022.117506>
- [23] Smith TR, Sugar JD, San Marchi Ch, Schoenung J (2021) Microstructural development in DED stainless steels: applying welding models to elucidate the impact of processing and alloy composition. *J Mat Sci* 56:762–780. <https://doi.org/10.1007/s10853-020-05232-y>
- [24] Yan F, Xiong W, Faierson EJ (2017) Grain structure control of additively manufactured metallic materials. *J Mat* 10:1260. <https://doi.org/10.3390/ma10111260>
- [25] Feenstra DR, Molotnikov A, Birbilis N (2020) Effect of energy density on the interface evolution of stainless steel 316L deposited upon INC 625 via directed energy deposition. *J Mater Sci* 55:13314–13328. <https://doi.org/10.1007/s10853-020-04913-y>

- [26] Carroll BE, Otis RA, Borgonia JP, Suh J, Dillon RP, Shapiro AA, Hofmann DC, Zi-Kui L, Beese AM (2016) Functionally graded material of 304L stainless steel and inconel 625 fabricated by directed energy deposition: characterization and thermodynamic modeling. *J Acta Mater* 108:46–54. <https://doi.org/10.1016/j.actamat.2016.02.019>
- [27] Li P, Gong Y, Xu Y, Qi Y, Sun Y, Zhang H (2019) Inconel-steel functionally bimetal materials by hybrid directed energy deposition and thermal milling: microstructure and mechanical properties. *Archiv Civ Mech Eng* 19:820–831. <https://doi.org/10.1016/j.acme.2019.03.002>
- [28] Yang SW, Yoon J, Lee H, Shim DS (2022) Defect of functionally graded material of inconel 718 and STS 316L fabricated by directed energy deposition and its effect on mechanical properties. *J Mater Res Technol* 17:478–497. <https://doi.org/10.1016/j.jmrt.2022.01.029>
- [29] Meng W, Zhang W, Yin X, Guo L, Cui B (2019) Additive fabrication of 316L/Inconel625/Ti6Al4V functionally graded materials by laser synchronous preheating. *J Int Jour Adv Man Tech* 104(5–8):2525–2538. <https://doi.org/10.1007/s00170-019-04061-x>
- [30] Han Q, Gu Y, Soe S, Lacan F, Setchi R (2020) Effect of hot cracking on the mechanical properties of Hastelloy X superalloy fabricated by laser powder bed fusion additive manufacturing. *Opt Laser Tech*. <https://doi.org/10.1016/j.optlastec.2019.105984>
- [31] Zhang X, Chai Z, Huabin Chen H, Xu J, Luming Ch, Lu X, Chen X (2021) A novel method to prevent cracking in directed energy deposition of Inconel 738 by in-situ doping Inconel 718. *J Mat Des* 197:109214. <https://doi.org/10.1016/j.matdes.2020.109214>
- [32] Kim SH, Lee H, Yeon SM, Aranas C Jr, Choi K, Yoon J, Yang SW, Lee H (2021) Selective compositional range exclusion via directed energy deposition to produce a defect-free Inconel 718/SS 316L functionally graded material. *Add Man* 47:102288. <https://doi.org/10.1016/j.addma.2021.102288>
- [33] Meng W, Zhang W, Zhang W, Yin X, Cui B (2020) Fabrication of steel-Inconel functionally graded materials by laser melting deposition integrating with laser synchronous preheating. *Opt Las Tech* 131:106451. <https://doi.org/10.1016/j.optlastec.2020.106451>
- [34] Dzugan J, Seifi M, Prochazka R, Rund M, Podany P, Konopik P, Lewandowski JJ (2018) Effects of thickness and orientation on the small scale fracture behaviour of additively manufactured Ti-6Al-4V. *Mater Char* 143:94–109. <https://doi.org/10.1016/j.matchar.2018.04.003>
- [35] Dzugan J, Prochazka R, Konopik P (2015) Micro-tensile test technique development and application to mechanical property determination. *STP 1576, ASTM Spec Tech Pub* 12–30. <https://doi.org/10.1520/STP157620140022>
- [36] Melzer D, Džugan J, Koukolíková M, Rzepa S, Dlouhý J, Brázda M, Bucki T (2022) Fracture characterisation of vertically build functionally graded 316L stainless steel with Inconel 718 deposited by directed energy deposition process. *Virt Phys Prot*. <https://doi.org/10.1080/17452759.2022.2073793>
- [37] Gushev M N, Busby J T, Field K G, Sokolov M A, Gray S E (2015) Role of scale factor during tensile testing of small specimens. *STP 1576, ASTM Spec Tech Pub* 31– 49. <https://doi.org/10.1520/STP157620140013>
- [38] Suzuki S, Sato S, Suzuki M, Kinoshita H, ato S, Jitsukawa S, Tanigawa H (2015) Influence of surface roughness on tensile strength of reduced-activation ferritic/martensitic steels using small specimens. *STP 1576, ASTM Spec Tech Pub*, pp 3–11. <https://doi.org/10.1520/STP157620140019>
- [39] Dzugan J, Sibr M, Konopik P, Prochazka R, Rund M (2017) Mechanical properties determination of AM components. *IOP Conf Ser Mater Sci Eng* 179:12019. <https://doi.org/10.1088/1757-899x/179/1/012019>
- [40] Azinpour E, Darabi R, Cesar de Sa JJ, Santos A, Hodek J, Dzugan J (2020) Fracture analysis in directed energy deposition (DED) manufactured 316L stainless steel using a phase-field approach. *Finite Elem Anal Des* 17715:103417. <https://doi.org/10.1016/j.finel.2020.103417>
- [41] Chvostová E, Horváth J, Konopik P, Rzepa S, Melzer D (2020) Optimization of test specimen dimensions for thermal power station exposure device. *IOP Conf Ser Mater Sci Eng* 723:12009. <https://doi.org/10.1088/1757-899x/723/1/012009>
- [42] Zerbst U et al (2021) Damage tolerant design of additively manufactured metallic components subjected to cyclic loading: state of the art and challenges. *J Prog Mat Sci* 121:100786. <https://doi.org/10.1016/j.pmatsci.2021.100786>
- [43] Pehlivan E et al (2020) Effects of build orientation and sample geometry on the mechanical response of miniature CP-Ti Grade 2 strut samples manufactured by laser powder bed fusion. *J Add Man* 35:101403. <https://doi.org/10.1016/j.addma.2020.101403>
- [44] Číhal V (1999) Corrosion-resistant steels and alloys. Academia, Czech Republic
- [45] Zheng B et al (2019) On the evolution of microstructure and defect control in 316L SS components fabricated via directed energy deposition. *J Mat Sci Eng A* 764:138243. <https://doi.org/10.1016/j.msea.2019.138243>
- [46] Yuan Z et al (2017) Additive manufacturing of 316L stainless steel by electron beam melting for nuclear fusion applications. *J Nuc Mat* 486:234–245. <https://doi.org/10.1016/j.jnucmat.2016.12.042>

- [47] Zietala M et al (2016) The microstructure, mechanical properties and corrosion resistance of 316 L stainless steel fabricated using laser engineered net shaping. *J Mat Sci Eng A* 677:1–10. <https://doi.org/10.1016/j.msea.2016.09.028>
- [48] Saboori A, Aversa A, Marchese g, Biamino S, Lombardi M, Fino P, (2019) Application of directed energy deposition-based additive manufacturing in repair. *Appl Sci* 9:3316. <https://doi.org/10.3390/app9163316>
- [49] Kiran A, Koukolíková M, Vavřík J, Urbánek M, Džugan J (2021) Base plate preheating effect on microstructure of 316L stainless steel single track deposition by directed energy deposition. *J Mat* 14:5129. <https://doi.org/10.3390/ma14185129>
- [50] Reichardt A, Dillon RP, Borgonia JP, Shapiro AA, McEnerney BW, Momose T, Hosemann P (2016) Development and characterization of Ti-6Al-4V to 304L stainless steel gradient components fabricated with laser deposition additive manufacturing. *Mater Des* 104:404–413. <https://doi.org/10.1016/j.matdes.2016.05.016>
- [51] Džugan J, Melzer D, Koukolíková M, Vavřík J, Seifi M (2020) characterization of functionally graded materials based on Inconel 718 and stainless steel 316L manufactured by DED process. *Struc Int Add Man Mat and Parts*, pp 247–256. <https://doi.org/10.1520/STP163120190138>
- [52] Dang X, Li Y, Chen K, Luo S, Liang X, He W (2022) Insight into the interfacial architecture of a hybrid additively-manufactured stainless steel/Ni-based superalloy bimetal. *Mater Des* 216:110595. <https://doi.org/10.1016/j.matdes.2022.110595>
- [53] Li Y, Dlouhý J, Koukolíková M, Kirana A, Vavřík J, Džugan J (2022) Effect of deposit thickness on microstructure and mechanical properties at ambient and elevated temperatures for Inconel 718 superalloy fabricated by directed energy deposition. *J All Com* 908:164723. <https://doi.org/10.1016/j.jallcom.2022.164723>
- [54] Prashanth KG, Scudino S, Maity T, Das J, Eckert J (2017) Is the energy density a reliable parameter for materials synthesis by selective laser melting. *J Mat Res Let* 5(6):386–390. <https://doi.org/10.1080/21663831.2017.1299808>
- [55] Liu SY (2020) The effect of energy density on texture and mechanical anisotropy in selective laser melted Inconel 718. *J Mat Des* 191:108642. <https://doi.org/10.1016/j.matdes.2020.108642>
- [56] Mei X, Wang X, Peng Y, Gu H, Zhong G, Yang S (2019) Interfacial characterization and mechanical properties of 316L stainless steel/inconel 718 manufactured by selective laser melting. *Mater Sci Eng A* 758:185–191. <https://doi.org/10.1016/j.msea.2019.05.011>
- [57] Wei H, Mazumder J, Debroy T (2015) Evolution of solidification texture during additive manufacturing. *Sci Rep* 5:16446. <https://doi.org/10.1038/srep16446>
- [58] Boyce BL, Clark BG, Lu P et al (2013) The morphology of tensile failure in tantalum. *Metall Mater Trans A* 44:4567–4580. <https://doi.org/10.1007/s11661-013-1814-8>
- [59] Havner K S (2004) On the onset of necking in the tensile test. *Int J Plast*:20, 4–5, 965–978. <https://doi.org/10.1016/j.ijplas.2003.05.004>

**Publisher's Note** Springer Nature remains neutral with regard to jurisdictional claims in published maps and institutional affiliations.